

# **Realizing a Dielectric Grating based Surface Plasmon Resonance Sensor**

by

Abhinav Ramakrishnan

Submitted to the Division of Engineering Science  
in partial fulfillment of the requirements for the degree of

Bachelor of Applied Science in Engineering Science

at the

UNIVERSITY OF TORONTO

June 2015

© Abhinav Ramakrishnan, MMXV. All rights reserved.

The author hereby grants to the University of Toronto permission to reproduce and to distribute publicly, paper and electronic copies of this thesis document in whole or in part, in any medium now known or hereafter created, for non-commercial purposes.

Author .....

Division of Engineering Science

April 9, 2015

# **Realizing a Dielectric Grating based Surface Plasmon Resonance Sensor**

by

Abhinav Ramakrishnan

Submitted to the Division of Engineering Science  
on April 9, 2015, in partial fulfillment of the  
requirements for the degree of  
Bachelor of Applied Science in Engineering Science

## **Abstract**

In this thesis an existing design for a multi-mode Dielectric Grating based Surface Plasmon Resonance (DGSPR) sensor is optimized, with respect to production and operation. To do the optimization, a simulation of the DGSPR structure (written in FORTRAN) was used, and parameters were varied manually, keeping key manufacturing considerations in mind. Due to limitations with regard to computational power, a simple iterative approach was used to perform the optimization.

Based on the optimized design, a master mold was be fabricated using a mixture of Electron-beam (E-beam) lithography and Deep Reactive Ion Etching (a Pseudo Bosch process). The final DGSPR master mold was examined under an electron microscope to determine the efficacy of the E-beam/DRIE process. The mold was found to have sufficiently smooth side-walls, and to have dimensions within 2% of the required values. A larger version of the proof-of-concept master mold can be used to repeatedly imprint pieces of  $SiO_2$  and hence create as many DGSPR configurations as required.

Thesis Supervisor: J. Stewart Aitchison  
Title: Professor (ECE)

## Acknowledgments

I would like to express my deepest gratitude to my supervisor Prof. Aitchison, for his guidance, support and most importantly his trust. We did not meet on a regular basis and he just had to trust that I was doing what I said I was doing. The lack of regular and constant supervision was a boon that I was very grateful for, as it gave me the space to experiment and play around with different ideas by myself, before ultimately running them through him.

I also want to thank Dr. Farshid Bahrami for taking the time to explain his idea to me, dumbed down quite significantly so that I could understand it. I'd also like to thank him for giving me his FORTRAN code - it was a great starting point and meant that a lot of the programming (which would have taken atleast an extra month to code) was already done, and that I could just go straight to the brute force search of the parameter space (after constraining it appropriately).

I also want to thank Arnab Dewanjee and Xiao Sun for the invaluable time and effort they expended in teaching me the basics of the various machines in the many clean rooms around the U of T campus. Were it not for them the SEM images in this thesis would never have existed, not to mention the quality of the fabricated structures would have been absolutely horrid.

I would also like to take this opportunity to thank Dr. Alexander Tsukernik and Dr. Edward Huaping Xu for their technical skills that they so generously offered.

I'm also indebted to my friend Adam Shaw who took the time to read over my thesis and point out the many many errors that I had made (a fair few of which were rather embarrassing).

Finally, I'd like to thank my parents for their constant love, support, and (when appropriate) criticism.

# Contents

<b>1</b>	<b>Introduction</b>	<b>1</b>
<b>2</b>	<b>Surface Plasmon Resonance Sensing</b>	<b>4</b>
2.1	Surface Plasmon Polaritons and SPR . . . . .	4
2.1.1	Surface Plasmon Resonance . . . . .	5
2.1.2	SPR Prism Geometries . . . . .	6
2.2	SPR Sensing . . . . .	11
2.2.1	SPR Bio-Sensing . . . . .	12
2.3	Motivation for a Dielectric Grating based SPR . . . . .	14
2.4	Summary . . . . .	15
<b>3</b>	<b>The DGSPR design &amp; optimization</b>	<b>16</b>
3.1	The DGSPR design . . . . .	16
3.2	Simulation . . . . .	18
3.2.1	Simulation Code . . . . .	19

3.3 Optimization . . . . .	20
3.3.1 Manufacturing considerations . . . . .	22
3.3.2 Low Accuracy Mass Analysis . . . . .	22
3.3.3 Mid Accuracy Select Analysis . . . . .	24
3.3.4 Extremely High Accuracy Analysis . . . . .	25
3.3.5 Results & Optimized Design . . . . .	27
3.4 Summary . . . . .	27
<b>4 NEMS manufacturing methods</b>	<b>29</b>
4.1 Lithography . . . . .	30
4.1.1 Deep UV Lithography (UVL) . . . . .	30
4.1.2 Electron Beam Lithography (EBL) . . . . .	32
4.1.3 Nano-Imprinting (NI) . . . . .	36
4.2 Proposed Manufacturing Method . . . . .	36
4.3 Summary . . . . .	40
<b>5 Process optimization of wall-e</b>	<b>41</b>
5.1 EBL process optimization . . . . .	42
5.2 DRIE process optimization . . . . .	47
5.3 Summary . . . . .	51

<b>6 Conclusion and Recommendations</b>	<b>54</b>
<b>Bibliography</b>	<b>58</b>

# List of Figures

2-1	Figure showing sub-critical total internal reflection . . . . .	7
2-2	Figure showing (a) the Otto prism configuration and (b) the Kretschmann prism configuration . . . . .	10
2-3	A typical flow based configuration for SPR bio-sensing (taken from [1]) . . .	13
2-4	A response-time graph of a typical SPR bio-sensing experiment (taken from [1])	14
3-1	Figure showing the DGSPR sensor design as in [2]. In (a) you can see a 3D blue-print of the DSGPR sensor and in (b) you can see a 2D cross-section of the same sensor. . . . .	17
3-2	Pythonic pseudo-code implementation of the integral aspects that comprise the DGSPR simulation . . . . .	20
3-3	Pythonic pseudo-code implementation of the support code called from the main function 3-2 . . . . .	21
3-4	Figure showing some examples of the results of low accuracy mass analysis with $h = 1.5 \mu m$ , $t_{Au} = 50 nm$ . . . . .	23
3-5	Figure showing more examples of the results of low accuracy mass analysis with $h = 1.5 \mu m$ , $t_{Au} = 50 nm$ . . . . .	24

3-6	Figure showing some examples of the results of mid accuracy analysis with $h = 1.5 \mu m$ , $\Lambda = 1200 nm$ , $t_{Au} = 50 nm$ and $\frac{w}{\Lambda} = 0.2$ . . . . .	25
3-7	Figure showing more examples of the results of mid accuracy analysis with $h = 1.5 \mu m$ , $\Lambda = 1200 nm$ , $t_{Au} = 50 nm$ and $\frac{w}{\Lambda} = 0.2$ . . . . .	26
3-8	Figure showing even more examples of the results of mid accuracy analysis with $h = 1.5 \mu m$ , $\Lambda = 1200 nm$ , $t_{Au} = 50 nm$ and $\frac{w}{\Lambda} = 0.2$ . . . . .	26
4-1	Figure showing an example of side-wall corrugation in Deep UVL. Image taken from [3] . . . . .	32
4-2	Figure showing an example of proximity effects in PMMA on Silicon. Image taken from [4]. . . . .	34
4-3	Figure showing a typical angle of both $x$ and $y$ stitching error. Image taken from [5]. . . . .	35
4-4	Figure showing a significant stitching defect in a grating. Image taken from [6].	35
4-5	Figure showing UVNI process. Image taken from [7]. . . . .	37
4-6	Figure showing smooth mold side-walls created using Yu's method. Image taken from [8]. . . . .	39
4-7	Figure showing smooth side-walls in imprinted resist using a mold created using Yu's method. Image taken from [8]. . . . .	39
5-1	Figure showing an example of an over-exposed ma-N grating pattern clearly exhibiting proximity effects . . . . .	43
5-2	Figure showing an example of an properly-exposed ma-N grating pattern . . .	43

5-3	Figure showing an SEM image of a properly-exposed ma-N grating pattern with an incorrect bias value. Note the smoothness of the grating. . . . .	44
5-4	Figure showing linear regression of beam dosage against proximity error correction values . . . . .	45
5-5	Figure showing resultant grating structure generated using a bias of $10\mu m$ and a dose of $500 \frac{\mu C}{cm^2}$ . . . . .	46
5-6	Figure showing under-developed grating structure after DRIE . . . . .	48
5-7	Figure showing perfectly-developed grating structure after DRIE . . . . .	49
5-8	Figure showing an example of improper stripping of ma-N after DRIE . . . . .	50
5-9	Figure showing an example of more proper stripping of ma-N after DRIE . . . . .	50
5-10	Figure showing an example of the irreparable damage caused by cleaving a structure . . . . .	51
5-11	Figure showing an example of the straight walls and the rectangular grating structure generated using the Pseudo Bosch process . . . . .	52
5-12	Figure showing an example of the smooth walls generated using the Pseudo Bosch process . . . . .	52

# List of Tables

3.1 Table showing the results of the High Accuracy Analysis i.e. the best possible configurations of the sensor for manufacturing . . . . .	27
---	----

# Chapter 1

## Introduction

A plasmon is a quantized unit of plasma vibration much like the phonon for mechanical excitations. Plasmonics is the study of these vibrations, particularly those arising from the coupling of light to free electrons in metals. An example would be the excitation of Surface Plasmon Polaritons (SPPs): by using light at the resonance frequency (matching k-vectors) any free electrons can be made to oscillate as a whole. SPPs are essentially guided surface waves (directed parallel to the metal interface) akin to light inside a fiber optic cable. This coupling of light to electrons in metals is inherently interesting since it allows for the breaking of the diffraction limit for the localization of light, thus allowing for light at higher wavelengths to resolve sub-wavelength features. Resonant excitations of SPPs known as ‘Surface Plasmon Resonance’ (SPR), are sensitive to variations in refractive index of various materials and as such could be very useful in bio-sensing applications.

An extremely useful feature of the SPR technique is the ability to detect extremely small refractive index variations near an interface. A sensor exploiting this ability is known as an affinity SPR sensor. Such sensors can be especially useful when dealing with bio-molecules since the concentrations of the molecules of interest are in the femtomolar range causing the time for analysis to be unfeasible. Over the years many improvements have been made regarding the use of affinity SPR sensors and it was found that the time for analysis could

be reduced significantly by using a flow-through geometry wherein the analyte solution was passed over the sensing surface [9].

Strictly speaking, in using the affinity sensor one simply aims to extract information regarding a thin bio-layer (adlayer) formed whilst using the flow-through geometry. However, the information required is coupled to other extraneous factors that cannot be separated as is. This arises from the evanescent-like nature of the SPP wave and its appreciable interaction with media beyond the thin adlayer (such as the bulk analyte solution itself). To this end a novel approach was suggested using a dielectric grating-based SPR (DGSPR) excitation. The DGSPR basically involves exciting 3 SPR modes instead of 1, hence gathering more data which could be used to decouple the useful information from the extraneous factors, consequently resulting in more accurate sensor measurements [2].

This thesis focuses on optimizing the existing DGSPR sensor's design with respect to general operating, manufacturing, and cost constraints; selecting a specific manufacturing method to use to fabricate the optimized DGSPR sensor; and optimizing the method used to fabricate the DGSPR sensor (in this case nano-imprint lithography was chosen) as much as possible within the given time constraints.

Fundamental to nano-imprint lithography is the concept of a master mold. The master mold is essentially a nano-scale stamp that can be pressed into a Silicon wafer to transfer a pattern. Due to the crucial nature of the master mold, this thesis focuses on the making of the master mold after which further work is needed on optimizing the stamping procedure (on which significant research has been done). With regard to the master mold, it is imperative that the pattern have the right dimensions, and that the side-walls, of the mold's grating structure, be smooth.

First, the pattern to be imprinted in the Silicon wafer is to be transferred to the master mold. This was done using electron beam lithography with attention being given to proximity effect correction (PEC). Due to the resist used in the fabrication process (ma-N), the PEC could not be done at the software end of the lithography process and was instead done manually by varying the beam current. The actual etching of the pattern was done using

a variant of Deep Reactive Ion Etching (DRIE) known as the Pseudo Bosch process. This resulted in a master mold that could in turn be used in nano-imprint lithography to generate the final DGSPR structure. In this thesis, due to both time and cost constraints, only a proof-of-concept prototype of the master mold was fabricated. This was sufficient to optimize the various individual processes used for fabrication.

A working master mold should allow for a working prototype which should in turn allow for the quick and easy diagnosis of a variety of diseases including AIDS (perhaps by monitoring CD40 membrane expression [10]). Such a device would have great use in the diagnosis and treatment of disease in countries such as Africa and India, where testing and monitoring for disease is usually unaffordable and time consuming for the general masses.

# Chapter 2

## Surface Plasmon Resonance Sensing

Surface Plasmon Resonance (SPR) Sensing is an optical technique used to determine a desired physical quantity using variations in the refractive index or variations in the absorption/reflection spectra. The SPR phenomena is in essence a charge density ( $\rho$ ) wave that may occur at the interface of two media that have permittivities of opposite sign (e.g. a metal-dielectric interface), when the interface is stimulated by incident light (obeying certain resonance conditions such as wave-vector matching). The coupled state is known as a Surface Plasmon Polariton (SPP). The charge-oscillation has an associated wave vector that achieves its maximum value at the interface and decays evanescently into the two media.

Based on which specific parameter is used to measure the variation in the SPR wave-vector, the SPR sensors can be classified into one of five categories: angle, wavelength, intensity, phase, or polarization modulation based SPR sensors.

### 2.1 Surface Plasmon Polaritons and SPR

A plasmon is a quantized unit of plasma vibration, similar to a phonon for mechanical vibrations. An example of plasma vibrations would be Surface Plasmon Polaritons (SPPs) which are generated by coupling light to electrons in an air-metal interface causing the free

electrons in the metal to oscillate as a whole. This type of coupling of light to electrons allows for the breaking of the diffraction limit for the localization of light, thus allowing for light at higher wavelengths to resolve sub-wavelength features.

Resonant excitation of SPPs (known as SPRs), are sensitive to variations in the refractive index of materials and as such are very useful in sensing applications. In particular, SPR sensing can be used to detect small fluctuations in the refractive index near the interface (where the SPR wave is the strongest); this particular configuration of the SPR sensor is known as an ‘affinity’ SPR sensor. Such a sensor is of great use when dealing with bio-molecules since “concentrations of analytes of interest in biological samples are in the femtomolar-to-nanomolar range” but “time required for analysis can be impractically long” [9]. However, as stated in [9], the process can be significantly expedited by using a flow-through geometry where the analyte solution is passed over the sensing surface - reducing the time taken for analysis.

### 2.1.1 Surface Plasmon Resonance

From hereon we will only be considering metal-dielectric interfaces. Other configurations are possible but remain outside the scope of this thesis.

The SPR phenomena is basically a free-electron wave excited by p-polarized incident light. This charge density oscillation is associated with an electromagnetic wave (known as the Surface Plasma Wave or SPW) which is also p-polarized. If we were to assume an interface between a semi-infinite dielectric and a semi-infinite metal, then the propagation constant of the SPW ( $\beta$ ) is given by:

$$\beta = k \sqrt{\frac{\epsilon_m n_s^2}{\epsilon_m + n_s^2}} \quad (2.1)$$

Where  $k$  is the free space wave number,  $\epsilon_m = \epsilon_{mr} + j\epsilon_{mi}$  is the relative permittivity of the

metal, and  $n_s$  is refractive index of the dielectric [11].

It is apparent from [Equation 2.1](#) that an SPR wave may be supported by a configuration as long as the denominator ( $\epsilon_m + n_s^2$ ) remains positive <sup>1</sup>. This condition is met by many combinations of metals and dielectrics, but the most common metals used are gold and silver. Note that the generated SPW is heavily concentrated in the dielectric region and less so in the metal region. This is mainly due to the high degree of attenuation experienced by the SPW in the metal. <sup>2</sup>

From [Equation 2.1](#) we may also get the skin depth ( $\delta_{skin}$ ) of the SPW - that is the distance over which the amplitude drops to  $\frac{1}{e}$  of its original value - given by:

$$\delta_{skin} = \frac{1}{\Im\{\beta\}} \quad (2.2)$$

### 2.1.2 SPR Prism Geometries

Due to the high degree of attenuation of the SPW in both the dielectric and metallic media - leading to a very limited penetration depth of the evanescent SPW - the sensing operation has to be carried out extremely close to the metal-dielectric interface. Thus it is essential that the system used to generate the SPW also be the system used to examine the SPR fluctuations. This has led to the development of extremely specialized SPR geometries.

#### Evanescent Waves

If a circular beam of light is incident onto a totally internally reflecting surface, it illuminates an ellipse on that surface. Only within the ellipse is an evanescent wave induced, i.e. an evanescent wave is induced only on the illuminated area of the totally internally reflecting

---

<sup>1</sup>Technically, the real part of the denominator should remain positive.

<sup>2</sup>There are some first order approximations of electrons in metals (based on the free electron model of an electron gas) that can be used to approximate  $\epsilon_m$ . It is however important to note that such models neglect attenuation.

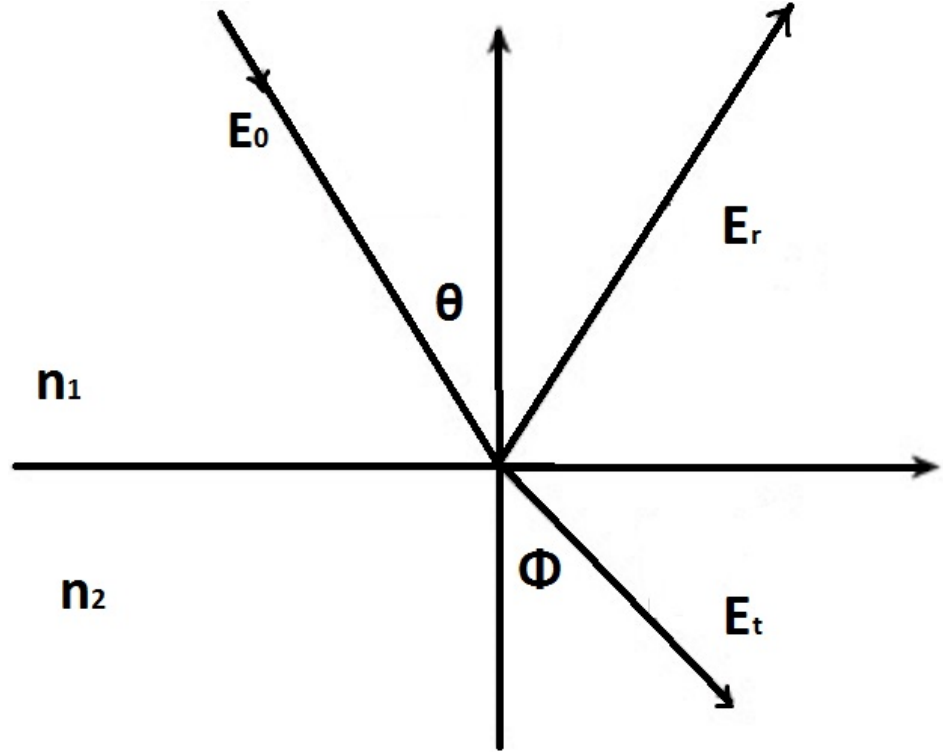


Figure 2-1: Figure showing sub-critical total internal reflection

surface. At the boundary of the illuminated surface exists a transitional area where the evanescent wave decays to zilch. The width of this transitional area is on the order of the incident light's wavelength.

For p-polarized incident light, the electric fields of the incident, reflected, and transmitted waves at an interface are not collinear. Careful application of Snell's law and the Fresnel equations immediately output the transmission & reflection characteristics for the sub-critical regime.

At the critical angle of the interface we find that this set of relations hold:

$$E_x = 0 \quad (2.3)$$

$$E_y = 2E_0 \quad (2.4)$$

$$E_z = 2\frac{n_1}{n_2}E_0 \quad (2.5)$$

Where  $n_1$ ,  $n_2$ ,  $E_0$  are the refractive indexes of the media surrounding the interface and incident electric field intensity respectively (as visible in Figure 2-1).

That  $E_z$  only depends on the refractive indexes of the media implies that choosing the media correctly would allow for the  $z$ -component of the evanescent wave to be stronger than the electric field of the incident wave [12]. Indeed, a simple calculation shows that in going from Silicon Dioxide ( $n = 1.4585$ ) to gold ( $n = 0.27049$ ) [13], there is approximately a 5-fold increase in the evanescent wave's strength compared to the incident wave.

Within the super-critical regime <sup>3</sup> it is sufficient to note that internal reflection is approximately total. It is exactly total for a non-absorbing rarer medium ( $n_2 < n_1$  and  $n_1, n_2 \in \Re$ ).

Furthermore, the evanescent wave thus formed travels along the interface extending slightly into the rarer media (in actuality it will also extend into the denser media but can be neglected to a first order approximation).

## Attenuated Total Reflection (ATR)

In reality, some of the evanescent wave is absorbed (due to complex refractive indexes) and thus the reflection is not really total. Simply put, the reflectance of the interface has troughs corresponding to those wavelengths that are absorbed by the rarer medium. At these specific wavelengths the total reflectance is said to be attenuated - hence the name Attenuated Total Reflection [12].

ATR Spectroscopy is similar to transmission spectroscopy and relies on the absorption of part of the evanescent wave by an absorbing material. That is, when an absorbing material is brought in contact with a totally reflecting interface, it absorbs some of the intensity of the evanescent wave and thus attenuates the reflected intensity. Profiling this reflected intensity allows one to generate an 'absorption' spectra and hence understand how optical parameters vary in the absorbing material.

---

<sup>3</sup> In this paragraph only with cases where the materials have real permittivities ( $n_1, n_2 \in \Re$ ) are dealt with.

Assuming that  $n_1 \in \Re$  and  $n_2 \in \mathbb{C}$ <sup>4</sup> we may derive the expression for the super-critical internal reflectance of p-polarized light:

$$R_p = \left| \frac{n_2^2 \cos \theta - j n_1 \sqrt{n_1^2 \sin^2 \theta - n_2^2}}{n_2^2 \cos \theta + j n_1 \sqrt{n_1^2 \sin^2 \theta - n_2^2}} \right|^2 \quad (2.6)$$

This equation is somewhat intractable and does not allow for in-depth understanding of the underlying physics. To gain a detailed understanding of absorption during super-critical internal reflection, there are less abstruse models such as the ‘Weak Absorption Model’ or the ‘Leaky Interface Model’ which barter accuracy for comprehensibility. An in-depth exploration of these models is provided in [12].

## ATR Prism Geometries

If we were to look again to Equation 2.1 and use the approximation that  $\epsilon_m \approx \epsilon_{mr}$ <sup>5</sup> then we see that Equation 2.7 holds (equality is achieved as  $k \rightarrow 0$ ).

$$\beta_{SP} = k \sqrt{\frac{\epsilon_{mr} n_s^2}{\epsilon_{mr} + n_s^2}} \geq \beta_{air} = kn_s \quad (2.7)$$

It is evident that in order to excite plasmons in a resonant fashion, the momentum of the incident light has to be enhanced to match the momentum of the SPW. This momentum enhancement can be engineered using ATR in prism couplers.

In the case of p-polarized light, the interaction may be simplified to incident light being passed through a prism made of glass to increase its momentum (and wave-number), so as to achieve resonance at a given wavelength & angle of incident. There are two main prism coupler variants - the ‘Otto’ configuration and the ‘Kretschmann’ configuration. Both are

---

<sup>4</sup>As with a metal-dielectric interface.

<sup>5</sup>This is equivalent to saying  $\Re\{\epsilon_m\} \approx \epsilon_m$ , which is a good approximation for metals since the imaginary component of  $\epsilon_m$  is usually very small.

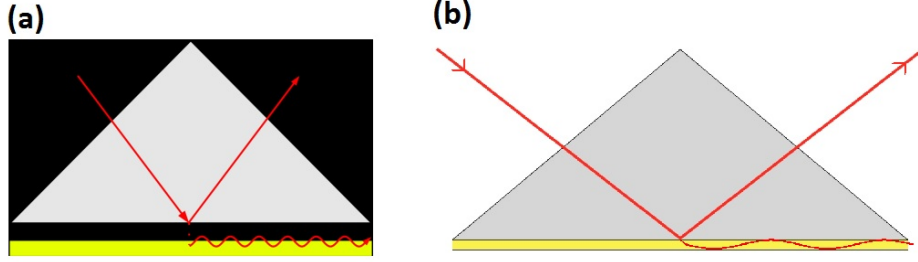


Figure 2-2: Figure showing (a) the Otto prism configuration and (b) the Kretschmann prism configuration

shown in [Figure 2-2](#)

The only significant difference between the Kretschmann setup and the Otto setup is the positioning of the metal film. In the Kretschmann setup the metal film is adhered onto the glass prism whereas, in the Otto setup, it is simply placed sufficiently close (a few 100 nm) so as to interact with the generated evanescent wave.

The equations governing the coupling of incident light to generate a SPP are simply a consequence of wave-vector matching:

$$\beta_{incident} = kn_{prism} \sin \theta_{SP} \quad (2.8)$$

$$\beta_{SP} = k \sqrt{\frac{\epsilon_m n_s^2}{\epsilon_m + n_s^2}} \quad (2.9)$$

Setting the above equations equal to each other results in <sup>6</sup>:

$$\Re \left\{ \sqrt{\frac{\epsilon_m n_s^2}{\epsilon_m + n_s^2}} \right\} = n_{prism} \sin \theta_{SP} \quad (2.10)$$

For completeness, the equation governing grating coupling (oriented with the grating surface in the x-direction) is also provided below<sup>7</sup>:

---

<sup>6</sup>A variant of this result, including the effects of grating coupling, is available in [2].

<sup>7</sup>The addition of grating coupling to prism coupling is a simple linear extension which will not be explained

$$\beta_x + mG = \beta'_{xm} \quad (2.11)$$

Where  $m \in \mathbb{Z}$ ,  $\beta_x$  is the component of the incident wave-vector along the grating surface, and  $G = \frac{2\pi}{\lambda_g}$  is the grating wave-vector ( $\lambda_g$  is the grating wave-length).

## 2.2 SPR Sensing

The principle behind SPR sensing is to use ATR to discern variations in the refractive index of the dielectric medium. The resonant excitation of the SPPs by incident light results in an SPW extending into the dielectric. Due to the large density of the SPW's field inside the dielectric under resonance conditions, the propagation constant (given by [Equation 2.1](#)) is extremely sensitive to variations in the optical properties of the dielectric adjacent to the metal layer supporting the SPW (we call this dielectric layer the transducing medium). Consequently, small fluctuations in the transducing medium can be detected via SPR sensing. The requirement that the transducing medium be adjacent to the metal layer is a result of the limited penetration depth of the SPW into the dielectric.

To put this more mathematically:

$$\delta\beta_{SP} = \frac{\partial\beta_{SP}}{\partial n_s} \delta n_s = \frac{kn_s(\epsilon_{mr} + j\epsilon_{mi})^2}{\sqrt{\frac{n_s^2(\epsilon_{mr} + j\epsilon_{mi})}{j\epsilon_{mi} + n_s^2 + \epsilon_{mr}}} (j\epsilon_{mi} + n_s^2 + \epsilon_{mr})^2} \delta n_s \quad (2.12)$$

Under the assumption that  $\epsilon_{mi}$  is negligible this gives:

$$\delta\beta_{SP} = \frac{k\epsilon_{mr}\sqrt{\frac{n_s^2\epsilon_{mr}}{n_s^2 + \epsilon_{mr}}}}{n_s^3 + n_s\epsilon_{mr}} \delta n_s \quad (2.13)$$

Using a Laurent expansion (about  $\epsilon_{mr} = \infty$ ) this can be simplified further to:

---

in detail in this thesis, but both are explained in great detail in [14] or [15] if required.

$$\delta\beta_{SP} = \frac{\partial\beta_{SP}}{\partial n_s}\delta n_s \approx k\delta n_s \quad (2.14)$$

So far we have only mentioned affinity sensors. To clarify, there are two main uses for SPR sensors: to discern variations within the ‘entire’ dielectric region - better known as bulk sensing; or to discern variations near the interface - better known as affinity sensing.

Based on which specific parameter is used to measure the variation in the SPR wave-vector<sup>8</sup>, the SPR sensors can be classified into one of five categories: angle, wavelength, intensity, phase, or polarization modulation based SPR sensors.

The five categories can be divided into roughly two sub-classes:

- Angle and wavelength modulation based sensors are primarily used to determine the resonance angle/wavelength at which a configuration has maximum coupling, ceterus paribus.
- Intensity, Phase and Polarization modulation based SPR sensing is used to profile the change in the intensity, the shift in the phase, or the variation in the polarization of the incident light which couples to the SPW, ceterus paribus.

### 2.2.1 SPR Bio-Sensing

Within the field of bio-sensing, SPR sensing has established itself as an extraordinarily powerful and quantitative probe of interactions which provides a means of identifying various interactions of bio-polymers. Further, SPR sensing also allows one to assign numerical values to various associated parameters such as: interaction equilibrium constants, interaction kinetic constants, and the intrinsic energetics of the various interactions.

A modified flow-based configuration based on the Kretschmann configuration is shown in [Figure 2-3](#). In the figure, a glass slide with a gold layer is adhered to a prism. Light passes

---

<sup>8</sup>The terms ‘wave-vector’ and ‘propagation constant’ are used interchangeably.

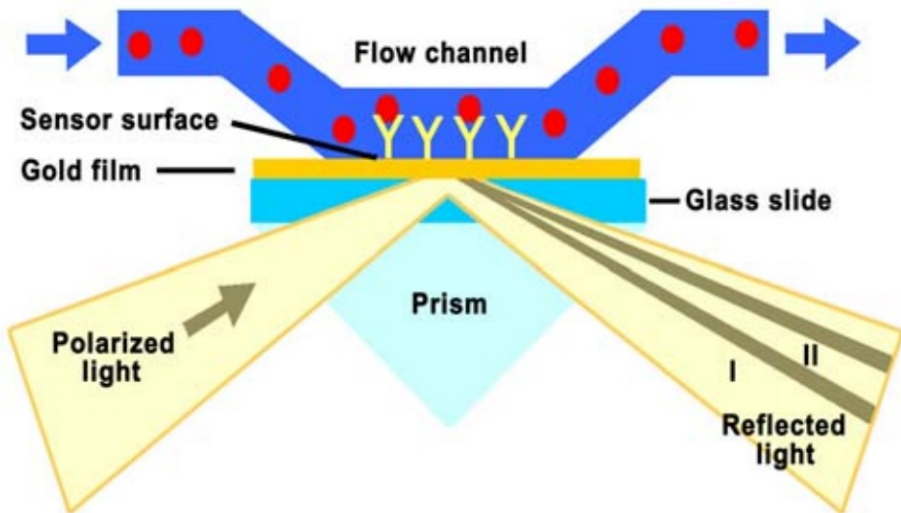


Figure 2-3: A typical flow based configuration for SPR bio-sensing (taken from [1])

through, couples to the gold-glass interface, reflects off the interface and passes back through the prism to a detector. Profiling the reflection against incident angle or wavelength gives a signal (real-time) proportional to the density of bio-polymer near the interface (in the adlayer).

The corresponding optical response vs. time graph (sensogram) is shown in [Figure 2-4](#). It is important to start with a stable baseline (generated by running pure buffer solution) against which one can compare variations in the optical response. The gold sensing surface is coated with targeted bio-receptors (mostly specific to single analyte molecule). Analyte molecules are injected and then left alone to achieve interaction equilibrium (the association stage - generating an adlayer). During this stage there may be a few molecules that non-specifically attach to the bio-receptors. To get rid of the non-targeted molecules that affixed themselves to the bio-receptors, the buffer solution is run through the system (we are now at the dissociation stage). At this point we should have pure dissociation as per Le Chatelier's principle ("If a dynamic equilibrium is disturbed by changing the conditions, the position of equilibrium moves to partially reverse the change."). We then have a regeneration stage to get the system back to its stable baseline.

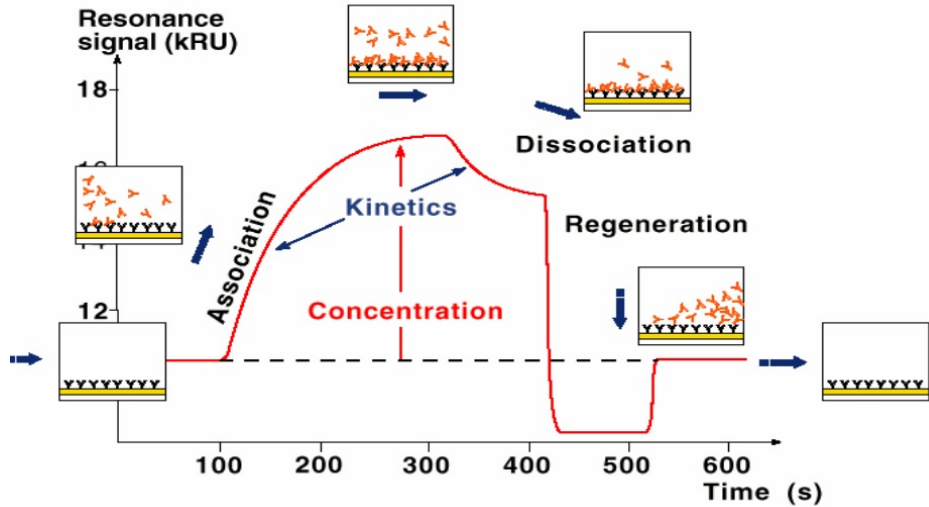


Figure 2-4: A response-time graph of a typical SPR bio-sensing experiment (taken from [1])

## 2.3 Motivation for a Dielectric Grating based SPR

In an SPR bio-sensor we aim to acquire information regarding the adlayer in the form of the adlayer's thickness ( $d_a$ ) and the adlayer's index of refraction ( $n_a$ ). However, the optical response of the SPR sensor also depends on factors such as the bulk analyte solution's index ( $n_b$ ). This is due to the evanescent nature of the SPW and its appreciable interaction with media beyond the thin adlayer. One way to decouple this information is to use an additional reference channel (to keep track of variations in  $n_b$ ). The main drawback of this ad-hoc method is that it's hard to implement and requires that every sensing channel be replicated as perfectly as possible, significantly hindering the use of the SPR sensor in high-throughput systems. Even if ideal conditions were somehow possible  $n_a$  still cannot be easily decoupled from  $d_a$  with a reference channel.

A Dielectric Grating based SPR (DGSPR) sensor is precisely what it sounds like. Developed by Bahrami et al., it's basically a Kretschmann configuration with an additional dielectric grating on top of the gold layer. This novel configuration allows for multiple stable SPR modes (you can achieve 3, 5, or even 7 mode spectroscopy). Given 3+ different continuous (or rather semi-continuous) measurements you can decouple  $d_a$ ,  $n_a$ , and  $n_b$  from each

other (if you use 7 modes then you could decouple a lot more extraneous factors). The only caveat with the DGSPR based sensor is that the normalized system matrix, i.e. the matrix containing the coupled set of differential equations that govern the sensing system, cannot be singular. This is easy enough to verify and the method to do so, along with an in-depth discussion of the DGSPR sensor, is provided in [2].

In this thesis, from here onward only the 3 mode configuration will be discussed (two p-polarized modes and one s-polarized mode). The other modes are theoretically possible but somewhat fiddly to actually realize and hence outside the scope of this thesis.

## 2.4 Summary

In this chapter a brief introduction to SPR based sensing has been provided along with the motivation for the DGSPR sensor. The next chapter will deal with the actual DGSPR design and its brute-force optimization.

# Chapter 3

## The DGSPR design & optimization

As mentioned in the previous chapter, Bahrami et al. came up with an innovative design (the DGSPR sensor) that allows for multiple stable SPR modes which can consequently be used in multi-mode spectroscopy to combat many of the problems faced by regular SPR sensing.

In this chapter, the novel DGSPR sensor will be examined in detail and the design parameters will be optimized with respect to operating & manufacturing constraints. Whenever ‘DGSPR’ is mentioned the structure discussed is identical to the one in [2].

### 3.1 The DGSPR design

The DGSPR design that we will examine in this thesis will be the 3 mode spectroscopy variant (two p-polarized modes and one s-polarized mode). This should allow for the decoupling of  $d_a$ ,  $n_a$ , and  $n_b$  from each other.

The DGSPR configuration consists of a SPR sensor affixed to a dielectric grating upon which targeted bio-receptors are placed. The metal (in this case gold was used) supports a p-polarized SPW whilst the dielectric gratings adds two more wave-guide modes (one p-

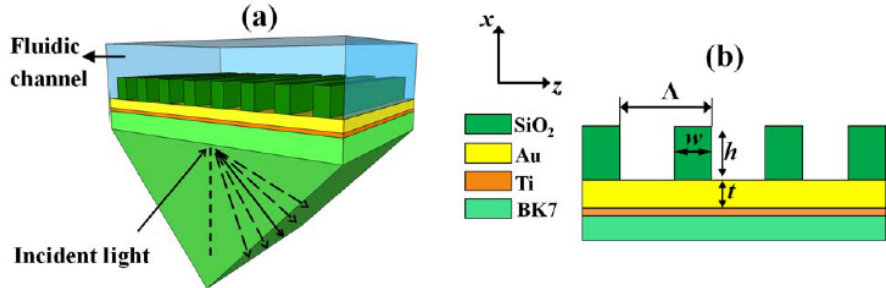


Figure 3-1: Figure showing the DGSPR sensor design as in [2]. In (a) you can see a 3D blue-print of the DSGPR sensor and in (b) you can see a 2D cross-section of the same sensor.

polarized and the other s-polarized). Thus there are 3 real-time measures to solve for 3 different real-time parameters (we are naturally assuming linearity - see [Equation 2.14](#); otherwise the problem might be intractable). Since we are only operating at a select wavelengths the dispersion characteristics are unimportant.

The DGSPR design is visible in [Figure 3-1](#). It is important to note that in the following analysis, the depth of the gratings as seen in [Figure 3-1](#) (a) are assumed to be infinite. This is a sufficiently good first order approximation. <sup>1</sup>

There is an interesting emergent property of the dielectric gratings placed on top of the gold in the DGSPR. In cases where we are interested in analyte solutions that contain molecules of various different sizes (such as in blood), the dielectric grating acts as an inbuilt filter allowing one to separately study larger and smaller molecules simultaneously. More exactly we can say this: “Molecules wider than  $\Lambda - w$  will only be found at a height greater than  $h$  from the gold surface (i.e. above the dielectric grating, in the bulk)”. This does not mean that smaller molecules do not exist in the bulk, only that larger molecules do not exist in the adlayer.

---

<sup>1</sup>One can argue that since we are assuming that the optical response is linear, analyzing the DGSPR structure in any greater detail than a first order approximation will not yield any significant gains in accuracy.

## 3.2 Simulation

The method used to simulate the DGSPR sensor was to model it using sensible first-order approximations to arrive at an approximate result. The accuracy of such an approximation then depends inversely on the step-size <sup>2</sup> and it's immediately obvious that the run time of such a simulation is directly proportional to the step-size (inversely proportional to the accuracy).

The first approximation is to consider the dielectric grating as a homogeneous medium with an average relative index as given in [16]. The zeroth order effective medium theory approximation gives:

$$n_s = \sqrt{fn_1^2 + (1-f)n_2^2} \quad (3.1)$$

$$n_p = \frac{1}{\sqrt{\frac{f}{n_1^2} + \frac{1-f}{n_2^2}}} \quad (3.2)$$

Where  $n_1$  and  $n_2$  are the indexes of the alternating slabs of dielectric that constitute the grating (with periodicity  $\Lambda$ ), and  $f$  is the volume fraction of the material with index  $n_1$  (in this case  $f = \frac{w}{\Lambda}$ ).

Using Equation 3.1 & Equation 3.2, we may replace the grating structure with a simple dielectric with a constant index( $n_{eff}$ ). This simplifies the DGSPR into a SPR, but one that can support two modes (similar to the Plasmon Wave-guide Resonance bio-sensor as discussed in [17]).

In using the zeroth order approximation we ignore the influence of the gratings. This can be remedied by using Rigorous-Coupled Wave Analysis (RCWA) to simulate the grating structure. In applying RCWA we end up right where we started, with an approximation that can support three modes.

---

<sup>2</sup>The larger the step-size, the larger the second-order (and higher-order) contributions.

To analyze the effectiveness of a particular configuration when applied to bio-sensing, we need a figure of merit (FoM) which in this case is defined by Bahrami et al. in [2] as:

$$CSF = SF \times SM \quad (3.3)$$

$$FoM = CSF_{surf,thick}^{p1} \times CSF_{surf,thick}^{p2} \times CSF_{bulk,index}^s \quad (3.4)$$

Where SM is the sensor merit, and SF is the sensor's sensitivity factor. The Combined Sensitivity Factor (CSF) is inversely proportional to the sensor's limit of detection. Thus it follows that the better the sensor, the larger the CSF.<sup>3</sup>

### 3.2.1 Simulation Code

The simulation code was written in FORTRAN 90 (this is the same code used by Farshid et al. in [2]) and the simulation method roughly follows the pseudo-code shown in [Figure 3-2](#) and [Figure 3-3](#).

There are a few things to keep in mind when reading this pseudo-code. In writing the code we have assumed infinitely deep gratings (in the y-direction in [Figure 3-1](#)), and an infinitely thick background.

Additionally, it should be mentioned that it is perfectly alright to have 3 different resonance angles (one for the s-mode and two for the p-modes) - this is not an expensive operation, and the system can be operated at 3 angles without any significant cost.

---

<sup>3</sup>The CSF is in essence of how ‘sharp’ the sensor’s resonance is, and can be calculated as the ratio of the resonance depth & the resonance FWHM. An in depth explanation of the definition of CSF is available in [18].

```

from backend import *
#This gives us all the required global constants such as: the various design parameters (Au, Ti & BK7
# thicknesses, Wavelength, Grating Height, Periodicity, Duty Cycle), the indexes of materials used,
# and the index of the background

def DGSPR_FoM(x, accuracy):
    # The main function. Note the inputs. X is a specific configuration of the system parameters
    # (Wavelength, Grating Height, Periodicity, Duty Cycle) and accuracy is the number of harmonics
    # The function returns the figure of merit along with various other useful results
    set_design_specs = x
    harmonics = accuracy
    #Get resonance parameters for all modes: Support Function
    width_no_ad, depth_no_ad, FWHM_no_ad = Adlayer(Adlayer_thickness = 0)
    width_ad, depth_ad, FWHM_ad = Adlayer(Adlayer_thickness = 2nm)

    #Calculate sensitivity and CSF values for all three modes: Support Function
    for mode in [p_mode_1, p_mode_2, s_mode]:
        SurfaceSens, CSF = depth_large(depth_mode_no_ad, depth_mode_ad)

    # At this point we should have 3 values for every calculated parameter
    # (2 corresponding to p-modes and 1 corresponding to a s-mode)

    FoM = max(CSF[p_mode_1, p_mode_2])*max(CSF[s_mode])
    Other = ['Incident Angles for Resonance', 'Sensitivity Factors',
             'Resonance Sharpness = (Res. Depth / Resonance Width)']
    return FoM, Other

```

Figure 3-2: Pythonic pseudo-code implementation of the integral aspects that comprise the DGSPR simulation

### 3.3 Optimization

The optimization of the DGSPR design is done by using methods disclosed in [section 3.2](#), and is aimed at maximizing the FoM defined in [Equation 3.3](#).

However, beyond the FoM, we also have to consider whether or not the final DGSPR sensor can be manufactured. This imposes certain additional criteria that we must recognize. It is also important to note that a DGSPR sensor must be comparable to a SPR sensor and as such, the values for the CSF-p and CSF-s must be atleast on the same order as those for an SPR sensor as given in [\[2\]](#).

For a given set  $X$  consisting of  $N$  different DGSPR configurations, the optimization of the design can be broken down into three sequential processes. Firstly, there is the low-accuracy analysis of all configurations in  $X$ . It is succeeded by the mid-accuracy analysis of select configurations that look promising. Finally we have the extremely accurate analysis of less

```

def Adlayer(Adlayer_thickness):
    #(55,85) is the critical region of the DGSPR sensor in most cases so...
    for angle in (55,85):
        # Return the FWHM parameters, depths, & widths of the resonances at all the different angles
        # for both the p modes and the s mode
        widths_arr, depths_arr, FWHM_parameters_arr = grating_FWHM_analysis(angle)
        for width in widths_arr:
            if width is reasonable:
                return width, depth, FWHM

def depth_large(depth_mode_no_ad, depth_mode_ad):
    for value in depth_mode_no_ad:
        if value > threshold:
            # If the resonance has a sufficiently Large depth w/o adlayer:
            depth_no_ad_large += value
    for value in depth_mode_ad:
        if value > threshold:
            # If the resonance has a sufficiently Large depth w/ adlayer:
            depth_ad_large += value

    # Values that generate a good resonance in both configurations (w/ & w/o adLayer):
    both = values in depth_ad_large and in depth_no_ad_large
    # Best possible resonance taking both w/ & w/o adlayer cases into account:
    best = max(both)
    return SurfaceSensitivity(best), CombinedSensitivityFactor(best)

```

Figure 3-3: Pythonic pseudo-code implementation of the support code called from the main function 3-2

than 3 configurations to select the best configuration in  $X$ .

Initially the optimization was done using genetic algorithms, but this was later found to be unfeasible due to a large majority of the results not being easily and/or cheaply manufacturable. Instead, the results of the genetic algorithm optimization process were used to constrain the parameter space for an exhaustive brute-force search. The constrained space obeyed the following rules:

- The wavelength was between  $700\text{nm}$  and  $1500\text{nm}$  (usually around  $770\text{nm}$ ).
- The duty cycle  $\frac{w}{\Lambda}$  was less than 0.55.
- The grating period  $\Lambda$  was less than  $1500\text{nm}$ .

- The grating height  $h$  was less than  $3\mu m$ .

In this way the parameter/design space was reduced to a much more manageable number of configurations ( $\sim 10,000$ ). Each configuration was then examined in turn in order to find the global optima.

### 3.3.1 Manufacturing considerations

Whilst the FoM characterizes the DGSPR sensor, some of the ‘good’ configurations output by a genetic algorithm based optimization routine are completely unfeasible due to not being manufacturable. Consequently, based on conversations with manufacturing companies specializing in Nano-Electro-Mechanical Systems (NEMS), a few general guidelines were devised: <sup>4</sup>

- The height ( $h$ ) of the gratings should increase in multiples of  $500nm$ .
- The width ( $w$ ) and the periodicity ( $\Lambda$ ) of the gratings should be multiples of  $100 nm$ .
- If  $w$  and  $\Lambda$  cannot be multiples of  $100 nm$ , then selecting them as multiples of  $50 nm$  is a viable, but less favorable, alternative.

### 3.3.2 Low Accuracy Mass Analysis

In the Low Accuracy Mass Analysis of many different combinations of grating period ( $\Lambda$ ) and duty cycle ( $\frac{w}{\Lambda}$ ), the accuracy was set to 2 harmonic orders. Furthermore, the FoM was modified such that it was 0 if it was not comparable to the SPR sensor or if the sensor did not support atleast 3 modes (2 p & 1 s).  $\lambda$  was set to be  $770nm$ .

---

<sup>4</sup>The cost of manufacturing the DGSPR sensor was also taken into account when devising the general guidelines.

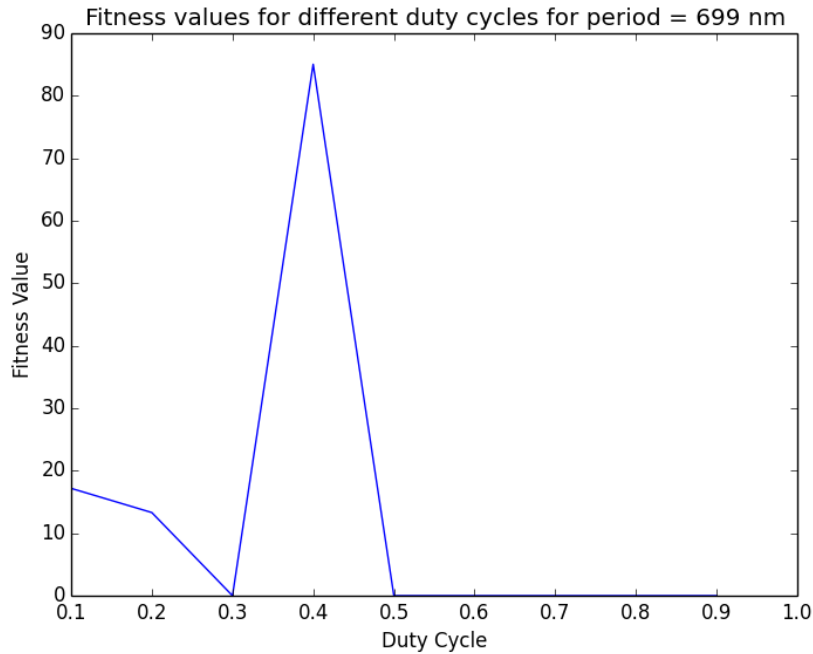


Figure 3-4: Figure showing some examples of the results of low accuracy mass analysis with  $h = 1.5 \mu m$ ,  $t_{Au} = 50 nm$

The period increased by  $100 nm$  between iterations, and the duty cycle varied between 0.1 and 0.9 in every iteration. All other variables such as grating height or incident wavelength were kept constant.

This was repeated for grating heights in  $\{1.0 \mu m, 1.5 \mu m, 2.0 \mu m\}$  - the grating height stepping size is  $500 nm$ , adhering to the general guidelines from before. The five best configurations corresponding to each grating height value were taken and analyzed further at a higher level of accuracy.<sup>5</sup>

This resulted in graphs such as those in [Figure 3-4](#) & [Figure 3-5](#).

---

<sup>5</sup>Examining the top two peaks would have been sufficient.

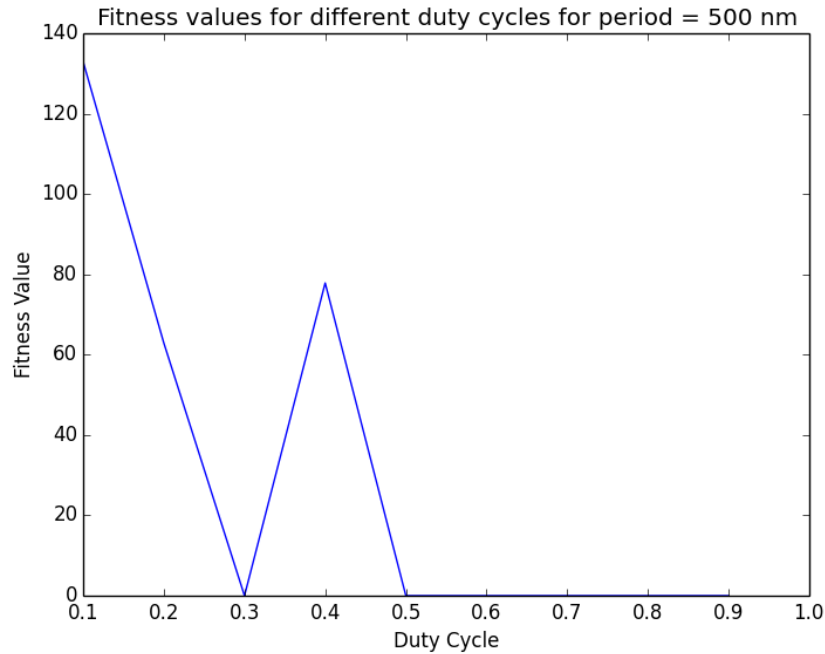


Figure 3-5: Figure showing more examples of the results of low accuracy mass analysis with  $h = 1.5 \mu m$ ,  $t_{Au} = 50 nm$

### 3.3.3 Mid Accuracy Select Analysis

In the Mid Accuracy Select Analysis of select combinations of grating period ( $\Lambda$ ), duty cycle ( $\frac{w}{\Lambda}$ ), and grating height  $h$ <sup>6</sup> the accuracy was set to 6 harmonic orders.

The previous modification to the FoM [it was 0 if it was not comparable to the SPR sensor or if the sensor did not support atleast 3 modes (2 p & 1 s)] was still used.

As stated earlier, the five best configurations corresponding to every value of grating height (as measured by FoM), were selected to be analyzed at mid-accuracy. For each configuration, the incident wavelength was varied so as to select the optimum operating wavelength for the DGSPR sensor. After the operating wavelength was identified, the duty cycle was perturbed slightly so as to get  $w$  to be a multiple of 100 nm or atleast a multiple of 50 nm.

---

<sup>6</sup>At this point it is interesting to note that exhaustive testing of configurations revealed that the other parameters identified by the genetic algorithm approach in [2] worked very well and there was no reason to deviate from them significantly. Indeed  $t_{Au} = 50 nm$  turned out to be the best possible value for most configurations. However, the incident wavelength did need some tuning.

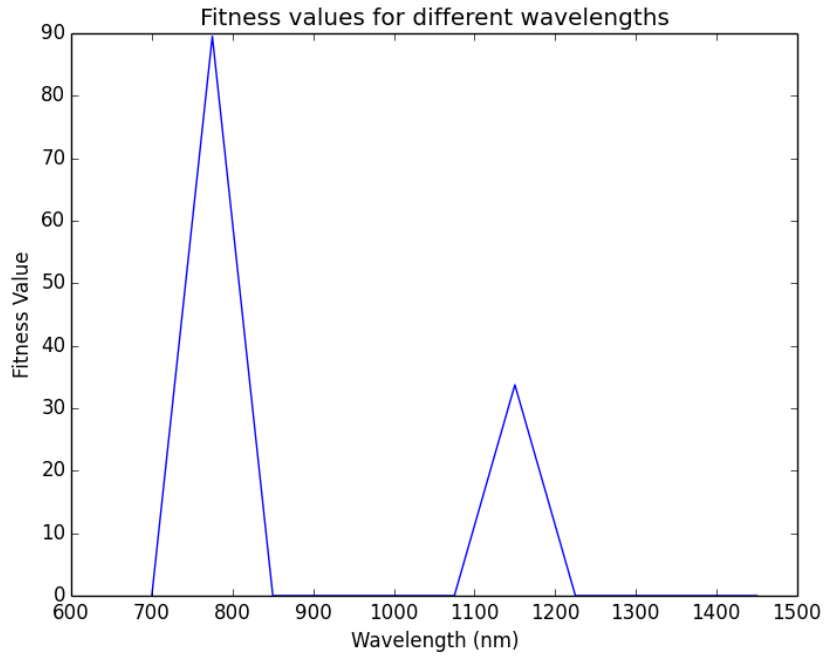


Figure 3-6: Figure showing some examples of the results of mid accuracy analysis with  $h = 1.5 \mu m$ ,  $\Lambda = 1200 nm$ ,  $t_{Au} = 50 nm$  and  $\frac{w}{\Lambda} = 0.2$

The best three configurations (which are alike in every way but for different duty cycles) were then taken forward to be analyzed at extremely high accuracy.

Mid-accuracy select analysis resulted in graphs such as those in [Figure 3-6](#), [Figure 3-7](#), and [Figure 3-8](#).

### 3.3.4 Extremely High Accuracy Analysis

In the Extremely High Accuracy Analysis of select combinations of grating period ( $\Lambda$ ), duty cycle ( $\frac{w}{\Lambda}$ ), and grating height  $h$ , the accuracy was set to 10 harmonic orders. The previous modification to the FoM still applied.

This step is not so much to get the best possible configuration possible, as it is to get reliable FoM values for a given configuration.<sup>7</sup> The best three configurations are then

---

<sup>7</sup>Reliability comes at a large cost - each configuration took about 10 minutes to run on an i5 with 4GB RAM.

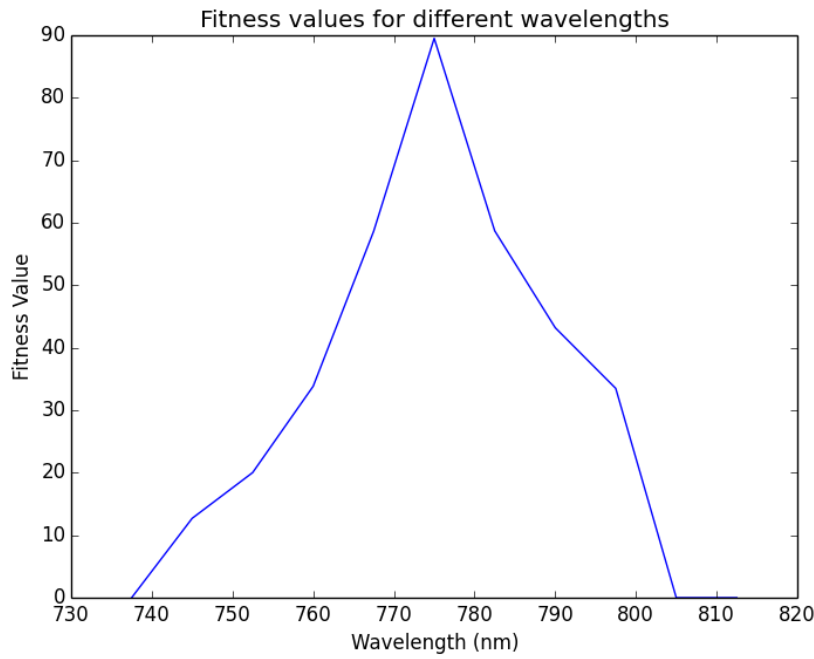


Figure 3-7: Figure showing more examples of the results of mid accuracy analysis with  $h = 1.5 \mu m$ ,  $\Lambda = 1200 nm$ ,  $t_{Au} = 50 nm$  and  $\frac{w}{\Lambda} = 0.2$

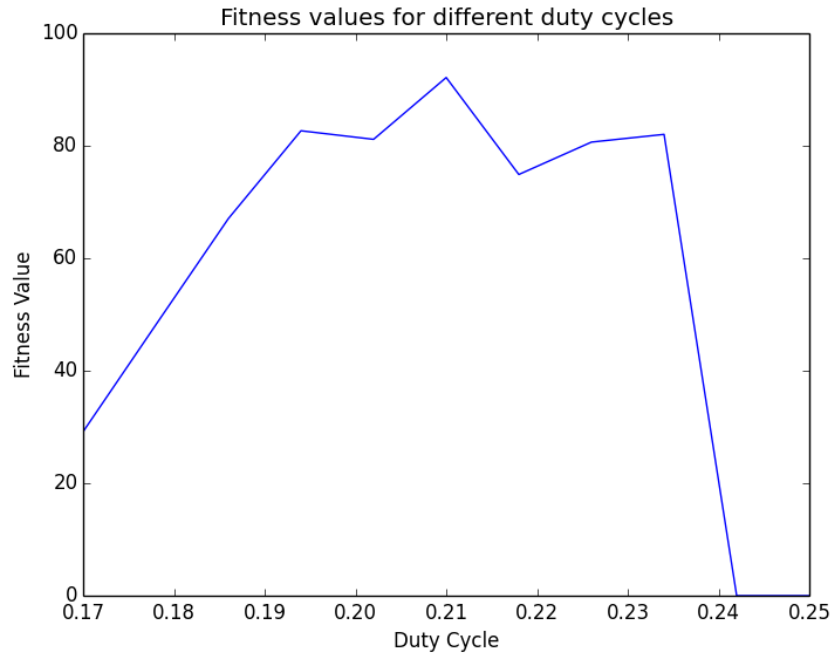


Figure 3-8: Figure showing even more examples of the results of mid accuracy analysis with  $h = 1.5 \mu m$ ,  $\Lambda = 1200 nm$ ,  $t_{Au} = 50 nm$  and  $\frac{w}{\Lambda} = 0.2$

compared against each other and the best configuration is selected.

High Accuracy Analysis basically resulted in trustworthy FoM numbers.

### 3.3.5 Results & Optimized Design

It is important to remember that this method of optimization will only provide local maxima for the FoM within the constrained design/parameter space. That is, all configurations that make it to the Extremely High Accuracy Analysis stage are the best configurations (constrained in the ways mentioned previously) within a certain neighborhood in the DGSPR parameter space. But, by comparing various local maxima to each other, if an exhaustive search of the constrained parameter space has been completed, one can be reasonably sure that the largest maxima is a global maxima.

The results of the High Accuracy Analysis are conglomerated in [Table 3.1](#)

Grating Height ( $\mu m$ )	Incident Wavelength (nm)	Grating Period (nm)	Duty Cycle	Grating Width (nm)	FoM
1.5	775	1200	0.20833	250	88.25143
1.5	782.5	1200	0.416667	500	99.445
2.0	760	1000	0.3	300	199.8923
2.0	787	500	0.5	250	32.09551
1.0	790	500	0.2	100	133.8602

Table 3.1: Table showing the results of the High Accuracy Analysis i.e. the best possible configurations of the sensor for manufacturing

The third configuration ( $h = 2.0$ ,  $\Lambda = 1000 \text{ nm}$ , and  $w = 300 \text{ nm}$ ) seems to be the global maxima and is what we will be discussing henceforth. It shall be known as the optimized design.

## 3.4 Summary

In this chapter a brief introduction to the DGSPR sensor, along with its design considerations, was provided. The method used to simulate the DGSPR was also explained and the optimization process was discussed in detail. Finally, an optimized design was discovered by

creating a fully spanning atlas of the design space using various localized maps. The next chapter will deal with the manufacturing methods used in the NEMS industry and will also decide which method should be used to actually manufacture the optimized design.

# Chapter 4

## NEMS manufacturing methods

In the previous chapter, the design of the DGSPR sensor was optimized with respect to operation & manufacturing based on simulations of the sensor, and conversations with NEMS manufacturers. In this chapter, three methods of NEMS manufacturing will be explored and the final method will be chosen such that the production process costs less than  $\sim \$ 5,000.00$ , can actually be completed within a reasonable time frame at the University of Toronto, and results in extremely smooth grating side-walls (which is imperative).

The NEMS methods that will be explored in this chapter are UV Lithography (UVL), Electron Beam Lithography (EBI), and Nano-Imprinting (NI). Each method has it's own advantages and disadvantages.

It is important to note that the actual design to be fabricated can either be the optimized design ( $h = 2.0 \mu m$ ,  $\Lambda = 1000 nm$ , and  $w = 300 nm$ ), or its negative ( $w = 700 nm$ ) depending on the NEMS method used.

## 4.1 Lithography

Lithography is by far one of the most common procedures in NEMS and relies on selectively removing parts of a ‘mask’ to generate a pattern mold. One then simply transfers that pattern over from the mask to a ‘resist’ (a material sensitive to a certain type of exposure) before developing the resist. Once the resist is developed, one may then etch the underlying substrate, consequently transferring the mask pattern over to the substrate.

Within lithography there are two main variants: Electron beam lithography and Ultraviolet based Photo-lithography. They differ mainly in the type of exposure used to develop the resist (and in other subtler ways), but they do also share many common operations.

### 4.1.1 Deep UV Lithography (UVL)

Also known as photo-lithography, UVL is one of the common methods used in the industry to generate micron & sub-micron length patterns (or in engineering terms - in the order of a few hundredths of a thou to a few thou). The resolution of the pattern is limited by the light used to develop the resist, the dimensions of the photo-mask, the aperture of the optical lens system, and various other process-related factors. It is a good estimate (upper bound) to say that the ‘critical dimension’ for the photo-lithography process is on the order of the wavelength of the light used <sup>1</sup>. Thus for UVL, the resolution is around  $\sim 150$  to  $200\text{ nm}$  (using wavelength values for far UV and middle UV).

The first step of the process is to make the photo-mask which contains the pattern which will be transferred onto the resist. It is theoretically possible to do mask-less UVL, using direct laser writing or maybe interference lithography, but these are limited in scope. Direct laser writing tends to have a large critical dimension (a few times larger than when using a mask), and interference lithography is limited to periodic patterns and truncated Fourier accuracy <sup>2</sup>.

---

<sup>1</sup>As an engineering rule of thumb one may use  $\frac{\lambda}{2}$  as an estimate for the critical dimension.

<sup>2</sup>If one were to Fourier transform a square wave and reconstruct it using only the first 7 harmonics of

The process of creating a mask (especially a simple periodic grating pattern) is best left to a commercial manufacturer - considering both the quality of the mask and the cost of making the mask - and will not be explained in detail. Such masks tend to cost around \$500 to \$1,000. To find such manufacturers one may consult [19].

To get the substrate ready for processing, one must coat it with a photo-resist. This is usually something like SU8, ZEP, or PMMA. To coat the substrate one may spin coat it with the resist. The thickness of the resist layer is completely controlled by the RPM and run time of the spin-coating operation. Once the substrate has been coated with resist it should be pre-baked (or ‘cured’) to get rid of excess.

Once the mask has been made (or bought), one must transfer the pattern over onto the photo-resist. This can be done by placing the mask on top of the resist, aligning it carefully with a mask-aligner, and then exposing the combination to light (usually UV). The resist will interact with the light and its molecular construction will change. After sufficient time exposing the resist to light, it can be ‘developed’ to remove only the unexposed resist (or only the exposed - depends on if positive or negative resist), leaving behind the pattern that was originally on the mask. This is then baked to harden the remaining resist, making it a better protective layer for the etching process.

After the resist has been developed, the substrate is ‘etched’. There are multiple ways to do the etching process (e.g. wet etch or ion-etching) but the fundamental idea is the same. The etching process removes the layers of the substrate that are not protected by the developed resist. The run-time of the etch is usually what controls the depth of the etching process, though there can be other influencing factors such as the voltage in DRIE.

After the etching process, the remaining resist is removed and one is left with a patterned substrate. A more in-depth discussion of the photo-lithography process is available in [20].

---

the sinusoidal reconstruction, the resultant square wave reconstruction would be significantly smoothed out. This is similar to what happens in interference lithography.

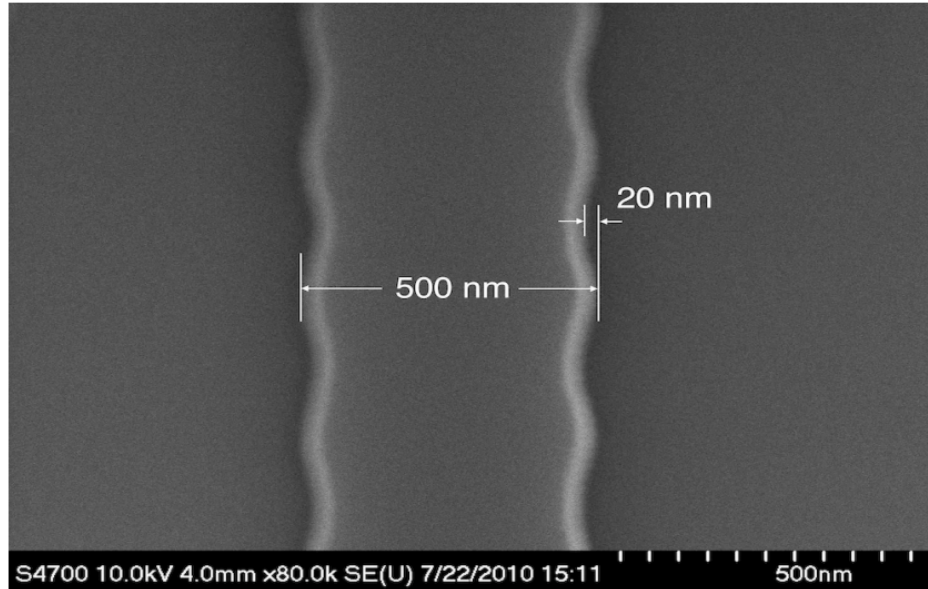


Figure 4-1: Figure showing an example of side-wall corrugation in Deep UVL. Image taken from [3]

### Issues with UVL

The larger the design, the more applicable UVL becomes. For patterns with smaller dimensions (on the same scale as the exposure wavelength) we get artifacts generated during the exposure process <sup>3</sup>. These in turn lead to etching errors on the scale of 10 to 20 nm. This is illustrated in Figure 4-1, where it is obvious that the walls of the grating pattern exhibit side-wall corrugation. Such artifacts are frequent in UVL.

Whilst UVL provides decent accuracy for sub-micron features, it comes into its own only for micron-scale features. Thus, for the purposes of manufacturing a DGSPR sensor, UVL does not satisfy the constraints.

#### 4.1.2 Electron Beam Lithography (EBL)

EBL shares much in common with UVL in that the method of developing the resist and etching are identical. The only real key change is that no mask is needed. The resist is

---

<sup>3</sup>An example of such an artifact is side wall corrugation as explored in [3].

placed on the substrate by spin-coating and is exposed directly to a moving electron beam which alters the resist's chemical makeup. The EBL method at the University of Toronto has a critical dimension of about  $10\text{ nm}$ .

The electron-beam has an extremely small ‘write-field’ which means that for large designs (anything over  $25\text{ nm} \times 25\text{ nm}$ ), the design will be broken into smaller quadrilaterals and each quadrilateral will be exposed one after the other.

After the design is exposed to the electron beam, the process of developing the resists and etching the substrate remains the same as with UVL.

The EBL system at the University of Toronto costs about \$400 per hour.

## Issues with EBL

It is important to note that there are a few additional, unwanted phenomena that occur with EBL. One such phenomenon is the forward scattering of the electrons as they pass through the resist, combined with the backwards scattering of the electrons from the substrate. This scattering causes the degradation of the pattern during exposure (shown in [Figure 4-2](#)). The degradation is due to the fact that any parts of the resist exposed to scattered electrons are also developed in conjunction with the intended pattern, thus causing significant variations. This degradation due to scattering can be modeled by a double Gaussian [21] (a sharp Gaussian to simulate forward scattering and a wide Gaussian to simulate back scattering) which is in turn called the proximity function. The degradation effect is hence called the ‘proximity effect’.

It is possible to correct for this using Proximity Effect Correction (PEC) by simulating proximity effects due to scattering before a design is exposed, and then altering the design dimensions or the exposure time/strength to counter the degradation. The PEC method and the algorithm used to reverse-engineer the effect are explained in [22] to great detail.

The University of Toronto recently invested in such a PEC system but no method is perfect

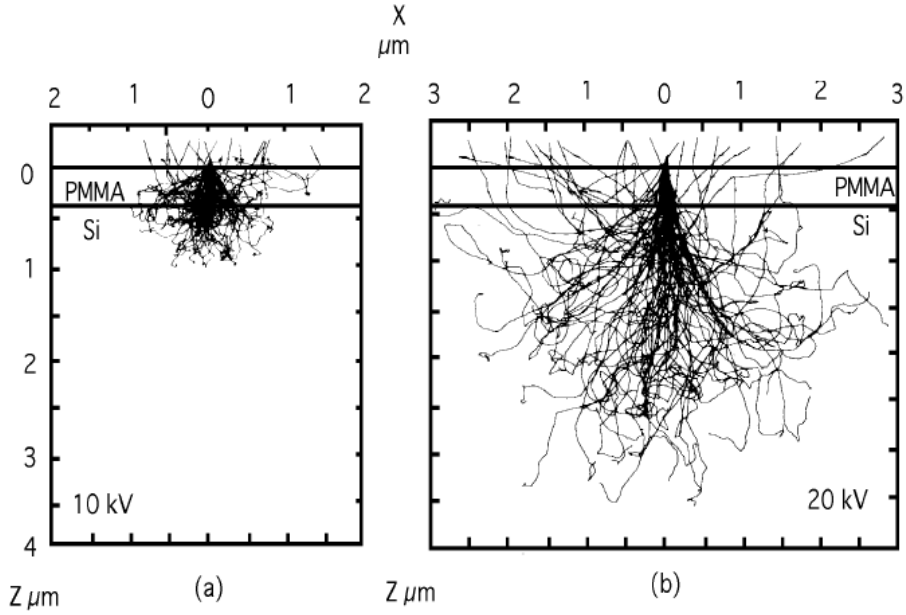


Figure 4-2: Figure showing an example of proximity effects in PMMA on Silicon. Image taken from [4].

and some degradation of the pattern should still be expected.

Another unwanted phenomenon is that of stitching error. Due to the vector-scan writing implementation used by most EBL systems, the overall pattern is created by stitching together many smaller write-fields. This causes something known as the stitching error which arises from the misalignment of various write fields. This is illustrated best using [Figure 4-3](#). The typical stitching error value in the machine used by the University of Toronto is  $25\text{ nm}$ .

The effects of stitching error usually compound quickly and tend to cause extremely significant, somewhat local, discontinuities in the pattern (as in [Figure 4-4](#)). Even applying specialized methods to minimize the stitching error (as explained in [6]) and taking the utmost care and precaution when using EBL, we can still only reduce the effects of stitching error to about  $10\text{ nm}$  (which has the potential to quickly multiply). The realistically way to minimize the effects of stitching error is to make the written pattern as wide as possible. An error of  $10\text{ nm}$  on something that  $1\text{ }\mu\text{m}$  wide is a lot less significant than the same error on something that's  $100\text{ nm}$  wide.

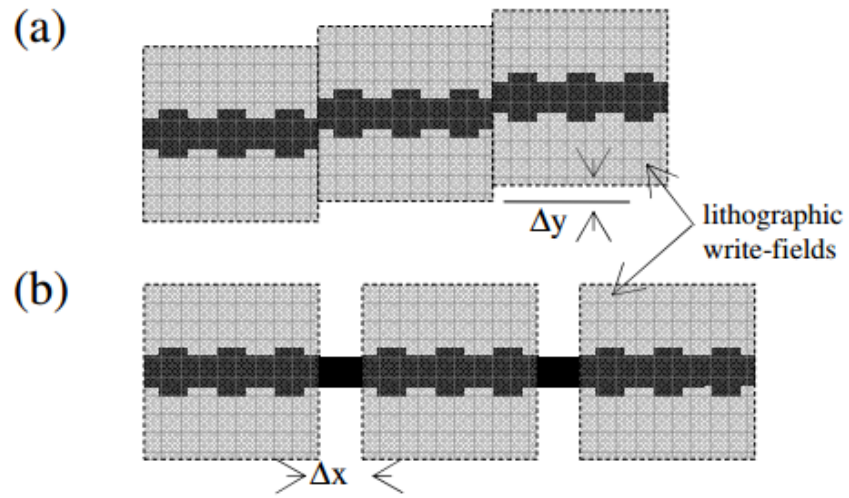


Figure 4-3: Figure showing a typical angle of both  $x$  and  $y$  stitching error. Image taken from [5].

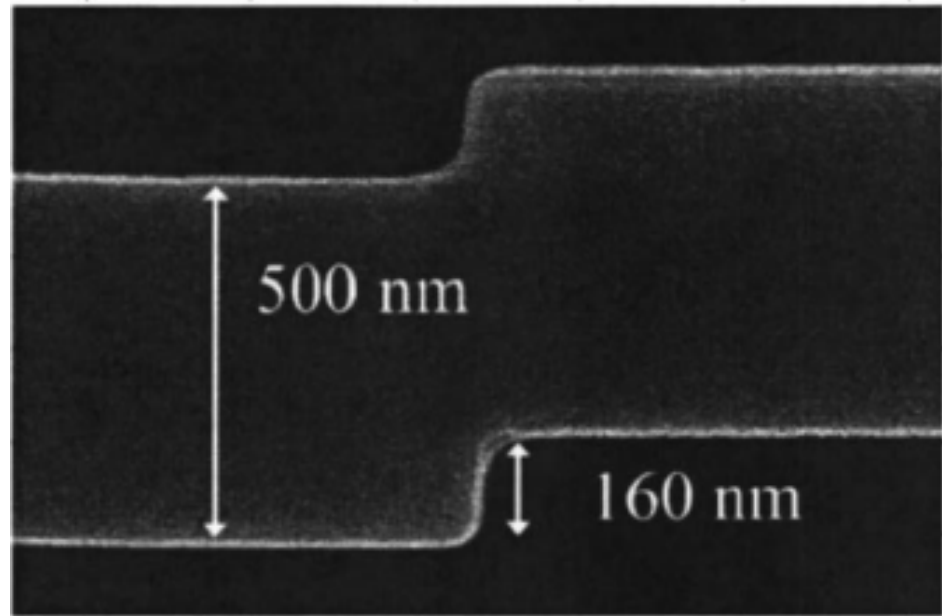


Figure 4-4: Figure showing a significant stitching defect in a grating. Image taken from [6].

The effect of all of these unwanted phenomena is that the walls of the exposed pattern, after developing & etching, tend to be somewhat rough - which cannot be tolerated in the manufacturing of the DGSPR.

#### 4.1.3 Nano-Imprinting (NI)

NI is based on mechanically modifying a resist to imprint a pattern. That is, NI uses direct contact between a ‘master’ mold and a resist to transfer a pattern from the master to the resist. Unlike with UVL or EBL, the process does not require any fancy equipment once the master has been made. It is cheap, easy to use. Furthermore, since NI uses direct contact, it overcomes the limitations set by light diffraction or beam scattering as in UVL or EBL.

There are two main variants of NI: Hot Embossing or Thermal NI (TNI), and UV cured NI (UVNI). In TNI, the resist is spin coated onto the substrate. The master is pushed into the resist and left there under a certain pressure. The resist is simultaneously heated up above the glass transition temperature. The system is then cooled and the master is removed. In UVNI (shown in [Figure 4-5](#)), instead of heating up the resist, UV light is shined through a transparent master to cure the resist thus transferring the pattern.

In both cases, once the pattern has been transferred the etching process can be started.

The resolution and fabrication quality achievable by NI for *nm* scale features far exceeds UVL. NI has similar resolution ( $\sim 10 \text{ nm}$ ) to EBL but, assuming the master mold has no significant defects, the imprinted pattern using NI will be of a better quality than with EBL (due to it being a contact process).

## 4.2 Proposed Manufacturing Method

After considering the constraints imposed at the beginning of this chapter - focusing mainly on the fact that the walls of the DGSPR’s grating need to be smooth - NI was selected.

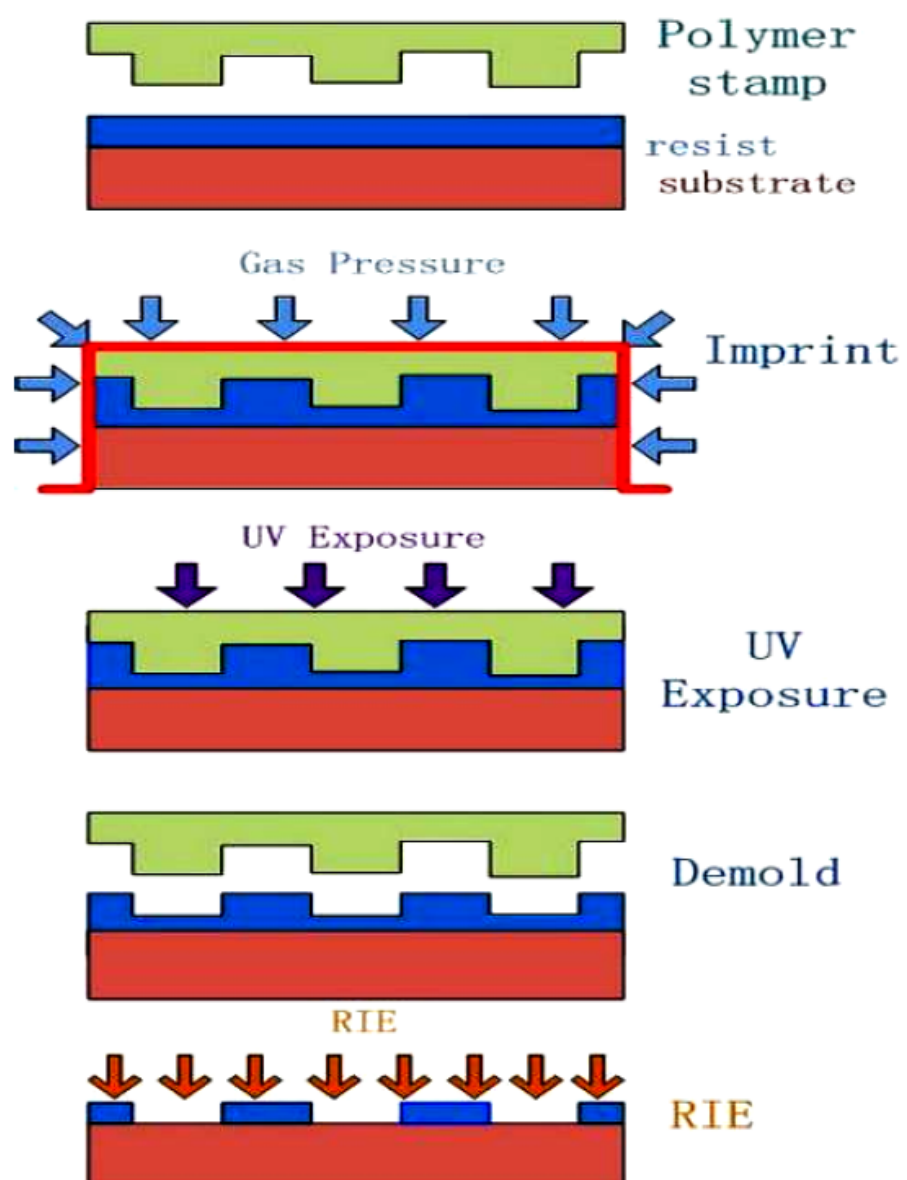


Figure 4-5: Figure showing UVNI process. Image taken from [7].

Thus the problem of producing the gratings reduces mainly to the problem of making the corresponding master mold and as such, the identified constraints will be applied to the making of the master mold instead of the complete DGSPR structure.

The method used to make the master mold is a combination of EBL, DRIE and wet-etching (if required). The selected method is a variant of a method described in the paper written by Yu et al. [8] and should result in a grating structure with extremely smooth side-walls.

Yu's method is aimed at creating a master mold for a grating structure in Silicon, using the inbuilt geometry of the Silicon crystal (i.e. using the fact that the crystal planes are practically perfectly straight). A (110) Silicon substrate is used as the mold surface and a layer of thick oxide is grown. The gratings are carefully aligned to the {111} reference flat of the Silicon crystal and etched using an Argon-Ion laser onto the thick  $SiO_2$  layer. The pattern is then transferred from the  $SiO_2$  layer, onto the Silicon (110) substrate using DRIE. If the walls are insufficiently smooth then a KOH wet-etch may be applied. Since the KOH wet-etch is extremely anisotropic (i.e. extremely slow in the ⟨111⟩ direction) this will result in extremely smooth side-walls. The entire process is explained in greater detail in [8]. The master mold created using this method, can then be used in the imprinting of other resists. Since the master has extremely smooth side-walls, so too do the imprinted resists. An example of a mold so created is visible in [Figure 4-6](#), and an example of an imprinted resist is visible in [Figure 4-7](#).

The variation on this method is to use EBL with negative resist to generate the grating pattern on top of the Silicon substrate. Once the grating pattern is generated, the etching of the Silicon master can be done using DRIE etching<sup>4</sup>. To smooth out any rough side-walls, a KOH wet-etch will be applied post DRIE (if required). This method will henceforth be known as the ‘smooth wall etching process’ or ‘wall-e’ for short.

---

<sup>4</sup>Theoretically, a Pseudo Bosch etching process should allow for extremely smooth nano-scale etching, making the KOH wet-etch step unnecessary.

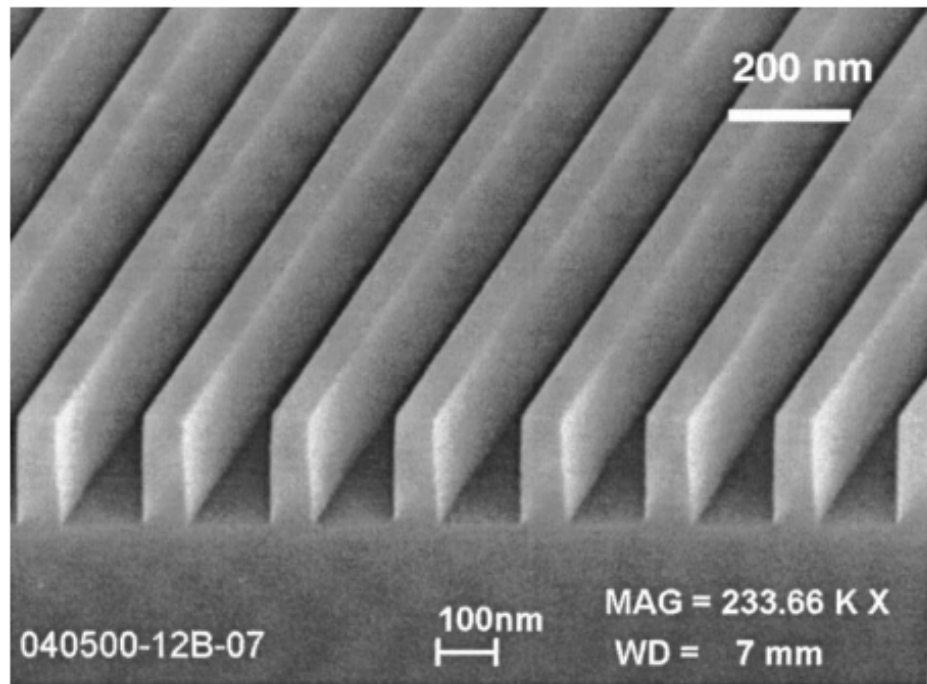


Figure 4-6: Figure showing smooth mold side-walls created using Yu's method. Image taken from [8].

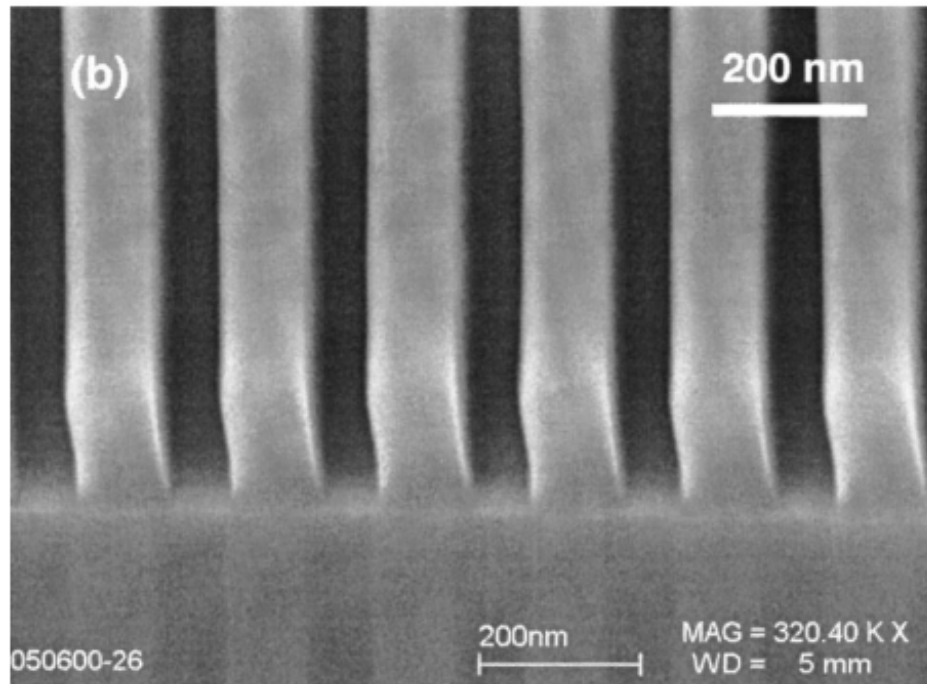


Figure 4-7: Figure showing smooth side-walls in imprinted resist using a mold created using Yu's method. Image taken from [8].

### **4.3 Summary**

In this chapter an overview of the three main NEMS manufacturing methods was provided and a method to actually fabricate a master mold (which will be used in turn to fabricate a DGSPR sensor using NI) was selected.

# Chapter 5

## Process optimization of wall-e

In the previous chapter, various NEMS manufacturing methods were examined, and a variation on a method used by Yu et al. in [8] was devised (called wall-e) to fabricate a DGSPR master mold. In this chapter, the various individual steps involved in the wall-e process will be optimized to result in a final mold with the required dimensions and smooth sidewalls. The dimensions of the master mold were taken to be: a periodicity of  $1000\text{nm}$ , a duty-cycle of 0.3, and a depth of  $2\mu\text{m}$ , identical to those of a DGSPR sensor. This is because there are multiple ways of actually applying the NI process (e.g. using a metallic shim attached to a rotor, using a smaller stamp along with micro-positioners), which means that both the optimized DGSPR design and its inverse are serviceable. In this case the optimized design with its 0.3 duty-cycle is harder to manufacture (due to having smaller dimensions) and as such its process was optimized. All of the various process optimizations within this chapter are still applicable to the inverse design but, due to its larger dimensions, may not be necessary.

The EBL and the DRIE processes in wall-e will be dealt with separately.

The proof-of-concept mold created was a  $100\mu\text{m} \times 100\mu\text{m}$  square on Silicon. It is the making of this mold that is discussed in the following sections.

## 5.1 EBL process optimization

To pattern the master mold, first the pattern (or its inverse in the case of a positive resist) must be ‘drawn’ onto a negative resist which is coated onto a plain silicon wafer. The resist must then be developed leaving behind a ‘mask’. The mask shields the underlying plain silicon wafer from the DRIE process after which it can be stripped off. The choice of a resist thus plays an important role in the DRIE process. Too weak a resist will not function well as a shield - the resist must exhibit the right ‘selectivity’ compared to Silicon. Moreover, due to the dimensions of the pattern to be formed, the chosen resist must also have the requisite resolution - otherwise the pattern cannot be drawn to any level of accuracy. The resist chosen, keeping in mind the aforementioned requirements, was ma-N 2405 [23].

The steps involved in using ma-N were simple. First a layer of HMDS was spin coated onto the silicon wafer at 5000 rpm for 15 seconds (to improve the adhesion between Si and ma-N), then the resist was spin-coated onto the wafer at 5000 rpm for 30 seconds, then the grating pattern with a width of  $300 - 2bnm$  ( $b$  is a bias term used for PEC) was drawn onto the resist using an electron beam, and finally the wafer was developed and examined under a scanning electron microscope (SEM) to ensure that it had the correct dimensions. A more detailed account of the steps required can be found on the Toronto Nanofabrication Center’s (TNFC) website (see [24]). The equipment used was the Vistec EBPG 5000+ Electron Beam Lithography System and its specifications can also be found on the TNFC website.

The first issue that developed was regarding the over-exposure of ma-N under the electron beam. In cases where the electron beam’s dosage/current exceeded  $600 \frac{\mu C}{cm^2}$  the resultant structure was over exposed and as a result there was a significant amount of proximity error easily visible in [Figure 5-1](#). Such extreme cases of proximity error may be thought of as beam ‘leakage’ causing neighboring patterns to overlap. In cases where the dose was less than  $600 \frac{\mu C}{cm^2}$  the pattern is clean and does not suffer much from beam-leakage as seen in [Figure 5-2](#). Under-exposure was also an issue and was solved by ensuring that the dose be above  $200 \frac{\mu C}{cm^2}$ .

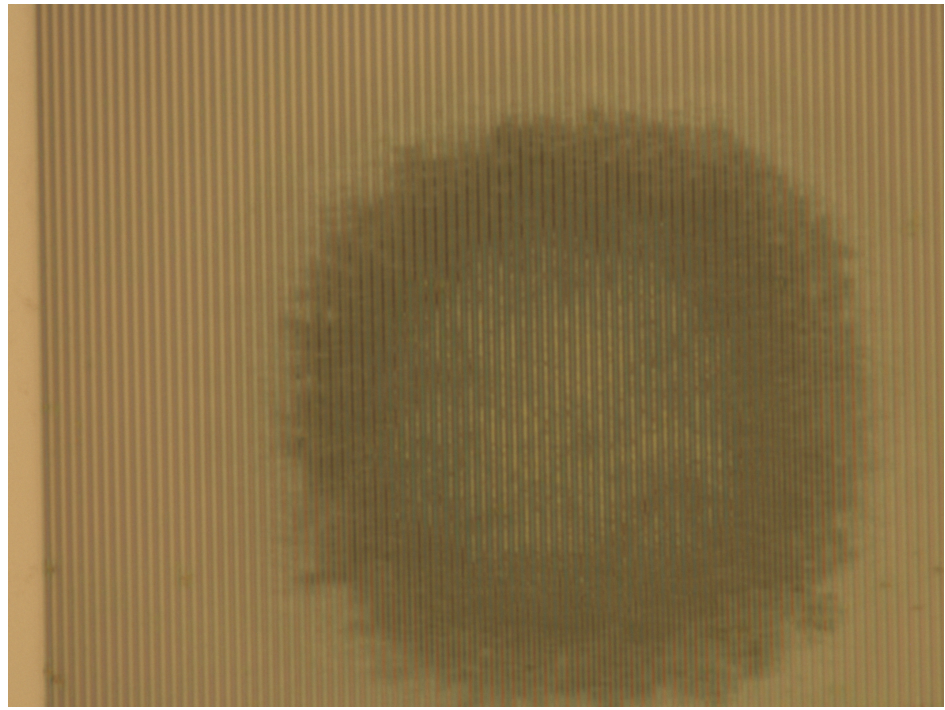


Figure 5-1: Figure showing an example of an over-exposed ma-N grating pattern clearly exhibiting proximity effects

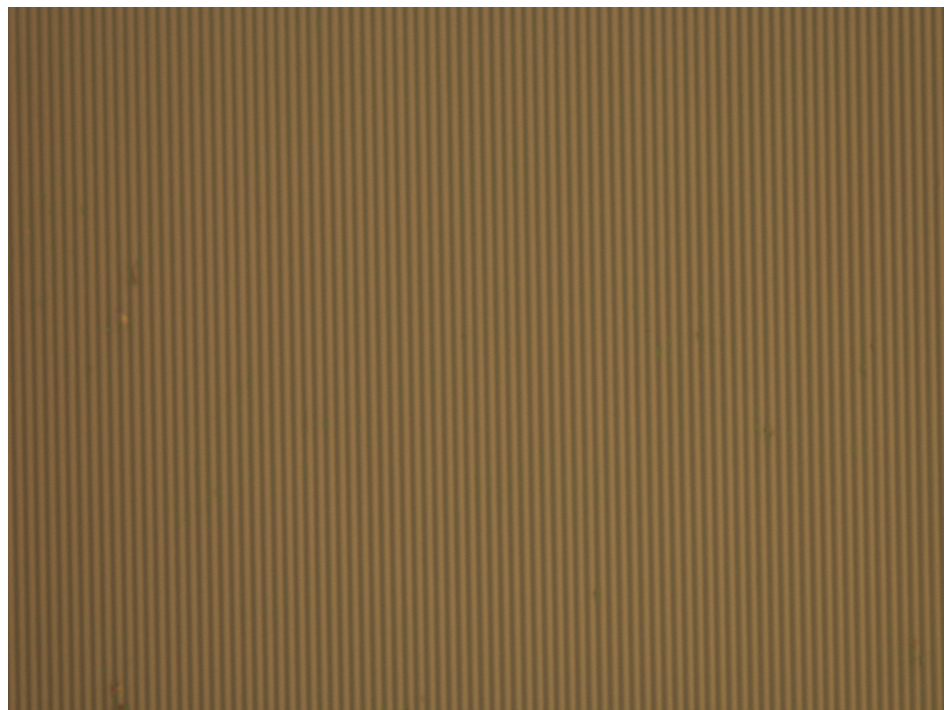


Figure 5-2: Figure showing an example of an properly-exposed ma-N grating pattern

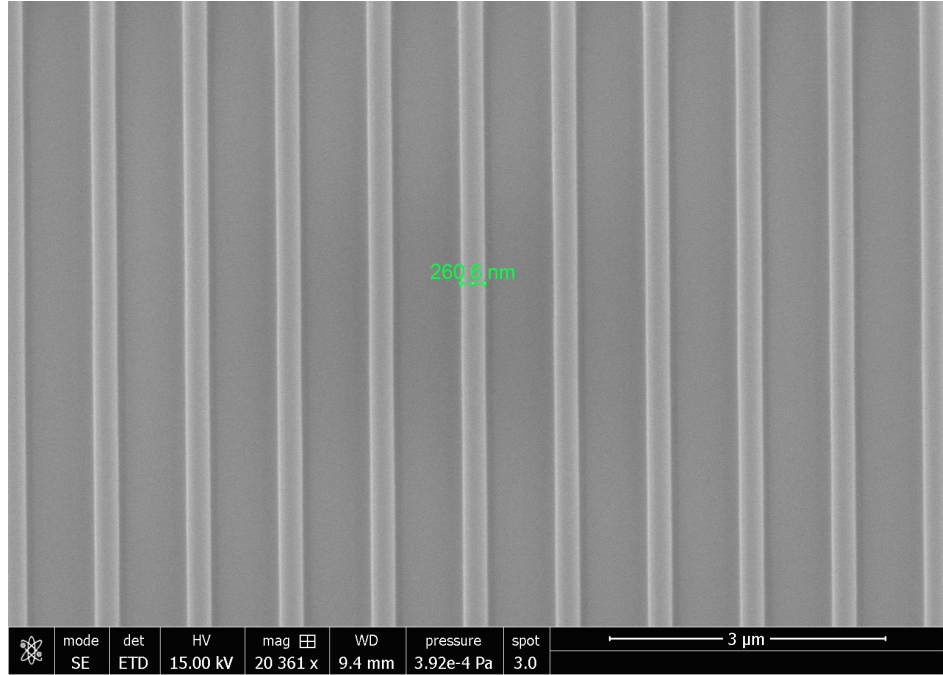


Figure 5-3: Figure showing an SEM image of a properly-exposed ma-N grating pattern with an incorrect bias value. Note the smoothness of the grating.

The second emergent issue was regarding the value of the bias term  $b$  that was used. The bias term is essentially a manual version of PEC. Hence, if  $b$  were chosen perfectly at  $10nm$ , then a  $280nm$  pattern would be drawn onto the ma-N, which due to proximity error effects, would end up being exactly  $300nm$ . The correct value of  $b$  thus depends on the dose used and should be chosen carefully. An example of an incorrectly chosen bias term is visible in [Figure 5-3](#) resulting in a structure with  $260nm$  wide gratings.

One may approximate the bias term required by using linear regression. First it is important to note that as a consequence of the width of the grating structure ( $300nm$ ), which is a few orders of magnitude larger than the beam diameter ( $\sim 10nm$  - see [25]), the beam has to traverse the width of each individual grating strip (as it covers the area of all of the gratings strips). This implies that the proximity error, visible at the edges of each grating strip, is directly related to the beam diameter which in turn means that the bias term is simply a function of the dose used. This implies that the same bias term would be required regardless of whether the grating had a thickness of  $700nm$  or  $120nm$  (atleast to within experimental accuracy). The proximity error effect is simply additive and dependent only on the beam

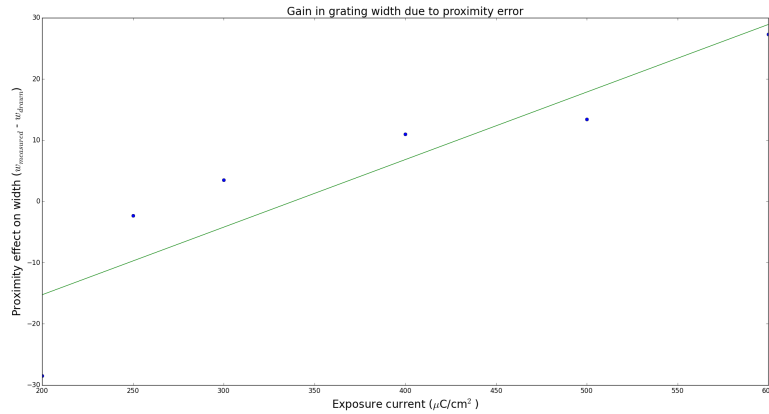


Figure 5-4: Figure showing linear regression of beam dosage against proximity error correction values

dosage. This has the added effect of explaining under-exposure which can be thought of as an additive effect as well.

It is then a simple matter to do a test run of a single bias value against various dosages, the results of which can be fit using linear regression. The resultant graph is shown in [Figure 5-4](#) for a bias value of  $25nm$  and various doses. The formula governing the linear regression fit is given in [Equation 5.1](#), where  $x$  is the dose in  $\frac{\mu C}{cm^2}$  and  $y$  is the additive correction ( $y = 2b$ ), from which the bias term may be extracted. The average absolute error between the data and the fit was  $6.43nm$  with a standard deviation of  $3.69nm$ . The fit had an  $R^2 = 0.814$  which is reasonable given the dearth of data points from the test run (each test run took about 4 hours to complete from the fracturing of the pattern to generate a GDS file - the only format the e-beam machine understands, to the development of the exposed structure).

$$y = 2b = 0.11036x - 37.31754 \quad (5.1)$$

Given the formula, one may reverse engineer it get the required dose for a given bias value. Applying it repeatedly to find ‘nice’ numbers for the bias value and dosage, one finds that these pairs serve well for (bias, dose):  $\{(10, 520), (12.5, 565), (15, 610)\}$ . Given the magnitude

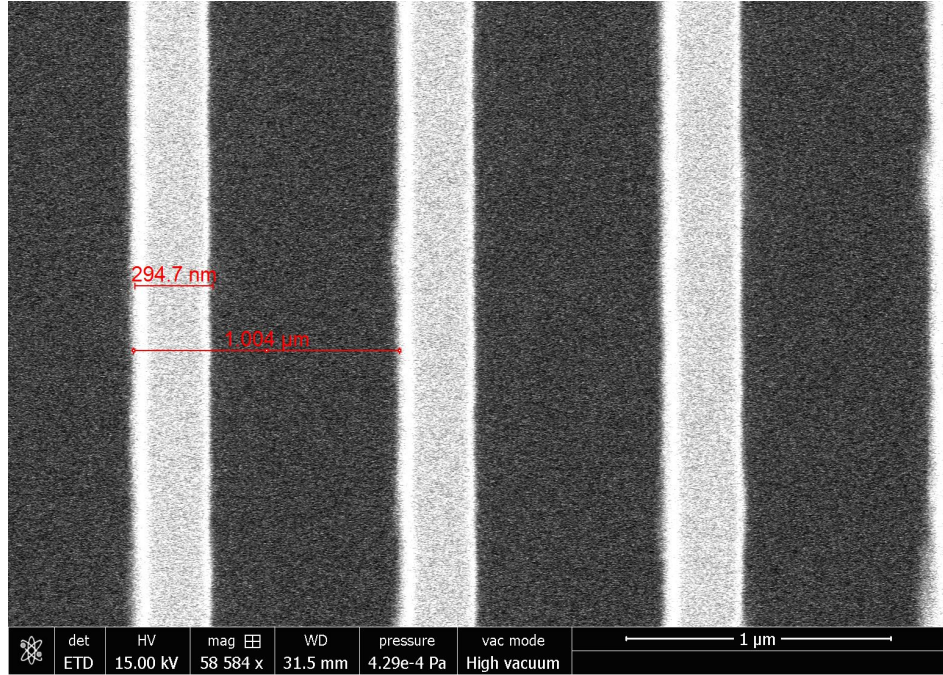


Figure 5-5: Figure showing resultant grating structure generated using a bias of  $10\mu m$  and a dose of  $500 \frac{\mu C}{cm^2}$

of the absolute error and the  $R^2$  value, there is no point in adhering to the calculated values strictly and as such the set  $\{(10, 500), (12.5, 550), (15, 600)\}$  may be used instead. Further, it would be advisable to try some similar, ‘local’ dose values for each pair as well. That is, for  $(10, 500)$  it would be advisable to explore all of  $\{(10, 450), (10, 500), (10, 550)\}$  i.e. dose  $\pm 50$ . An example of the results of such a method are shown in Figure 5-5 which was run at a bias of  $10\mu m$  and a dose of  $500 \frac{\mu C}{cm^2}$ .

The final important issue that arose was the developing time of the exposed ma-N resist. The ma-D developer solution dissolves exposed and unexposed ma-N resist at different rates, thus if the ma-N resist structure is left in the developer for too long then the pattern will simply be dissolved away. However, if the ma-N is not left in the developer for long enough then the structure will not be sufficiently ‘clean’ which in turn will affect the resolution of the following etch process. The suggested time to immerse in the developer was 2-4 minutes but 6.5 minutes seemed to work best. Any more and there was risk of compromising the dimensions of the pattern.

Having followed all of these ad-hoc tweaks, the Silicon wafer with a patterned mask was finally ready for DRIE.

## 5.2 DRIE process optimization

The Bosch etching process is a common etching process that uses Fluorine based plasma chemistry (using  $SF_6$ ) in an etch step to slightly etch the non-masked Silicon substrate. It then uses a Fluorocarbon plasma procedure (using  $C_4F_8$ ) in another step to develop a side-wall passivation layer to ensure that further etching of the same side-wall section does not occur. These two steps are repeated until the desired etch depth is reached. The Bosch process is not, in and of itself, good for nano-scale etching. The DRIE process that was actually used to etch the grating structure is a variant of the Bosch process commonly known as the Pseudo Bosch process or the mixed etching process. In essence it is a variant of the Bosch process wherein  $SF_6$  is mixed in the same step as  $C_4F_8$ . The Bosch Process and the Pseudo Bosch process are explained in greater detail in [26]. It is also useful to read [27], wherein the Bosch, Pseudo-Bosch, and Cryo processes are compared against each other; the processes are performed using same equipment available in the clean rooms of U of T. There is a certain roughness due to scalloping in the Bosch process, but this can be minimized significantly by using a low etch rate (rapid cycling between steps). Done at a low enough etch rate (high enough cycling rate) the induced side-wall scalloping roughness can be reduced to  $\sim 15nm$  - it may be slightly more or slightly less but this can not be determined given the quality of the SEM images.

The depth of the etch process is unimportant for the most part. The quality of the etch does not change with depth. To get the right depth one must simply experiment with the process time - this can only be done through trial and error. The use of an average etch rate is useless given the fact that the actual etch rate varies depend on the configuration that is being etched. With regard to the proof-of-concept mold, the average depth was  $1.3\mu m$ . The equipment used was the Oxford Instruments PlasmaPro Estrelas 100 DRIE System and its

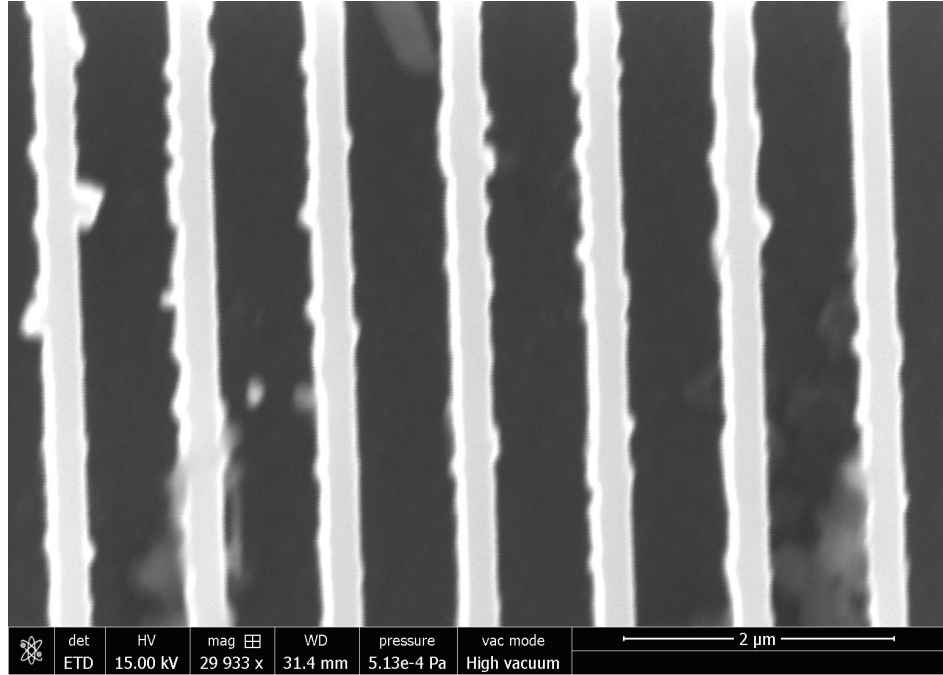


Figure 5-6: Figure showing under-developed grating structure after DRIE

specifications are available on the TNFC website ([28]).

There were two main issues that arose regarding the DRIE process. Firstly, was the consequences of not developing the ma-N resist correctly. If the ma-N resist is not developed sufficiently (i.e. developed in ma-D for less than 6.5 minutes) then the gratings are not smooth, which can be ascribed to the unwanted remnant resist. This is clearly visible in Figure 5-6. This should be contrasted against the perfectly developed structure which results in smooth gratings such as those in Figure 5-7.

The second issue was the result of improper stripping. After structure is etched using DRIE the remaining resist needs to be washed off. In the case of ma-N this is done using acetone. It is essential that this process be done for long enough (similar to the development of ma-N) and it was found that  $\sim 20$  minutes worked best. After this process a simple rinse under isopropanol would ensure there was no organic residue clinging to the master mold. It is imperative that the structure not experience any forces whatsoever. The features on the grating structure have an aspect ratio  $> 2$  which makes them significantly unstable (the

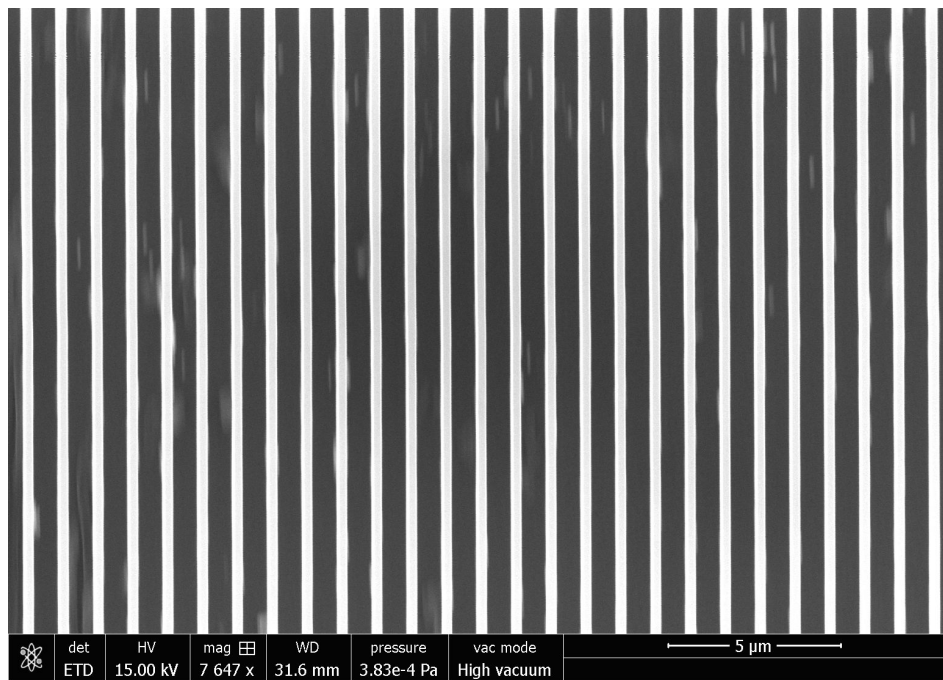


Figure 5-7: Figure showing perfectly-developed grating structure after DRIE

features are appreciably taller than they are wide) and likely to topple over.<sup>1</sup> An example of the results of the improper stripping of ma-N is visible in Figure 5-8, wherein significant physical damage to the grating structure is observable (in particular an entire grating strip has completely detached). An example of the results of a more proper stripping of ma-N is visible in Figure 5-9, wherein there is still some physical damage to the grating structure, but nothing quite so severe as in Figure 5-8.<sup>2</sup>

Once a sample has been properly developed and (mostly) properly stripped, as in Figure 5-7, it needs to be cleaved before a cross-section can be seen. In cleaving the sample one cuts right through the grating structure, perpendicular to the direction of the grating (along the direction of the grating's width axis), thereby causing irreparable damage to the original structure. It is important to note before viewing a cross-section that there may be residue of the ma-N resist. These are artifacts and do not influence the actual structure. These artifacts could be removed by leaving the sample overnight in a stripping solution (or over the course of multiple days, ensuring that the stripping solution is renewed often). An example of the

---

<sup>1</sup>This was particularly hard to address since the experimenter had extremely shaky hands.

<sup>2</sup>To get even better ma-N stripping required more time and steadier hands, neither of which were available.

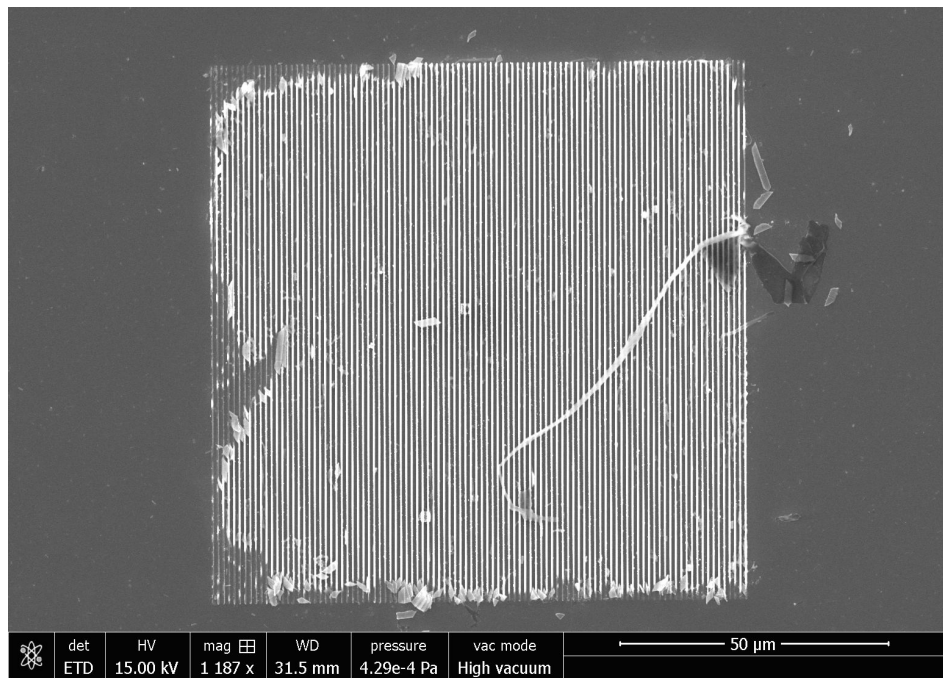


Figure 5-8: Figure showing an example of improper stripping of ma-N after DRIE

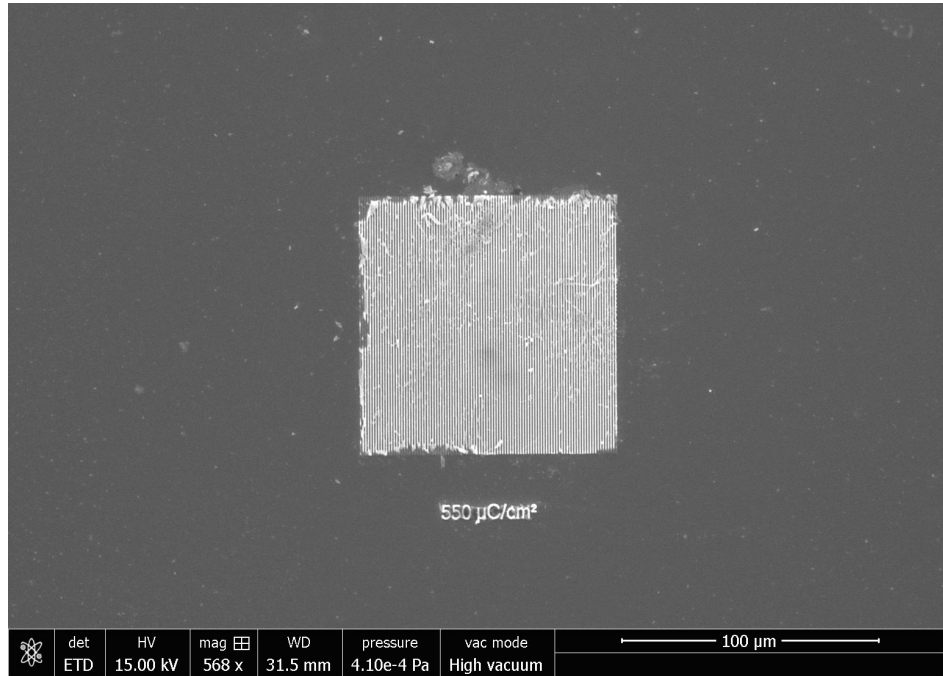


Figure 5-9: Figure showing an example of more proper stripping of ma-N after DRIE

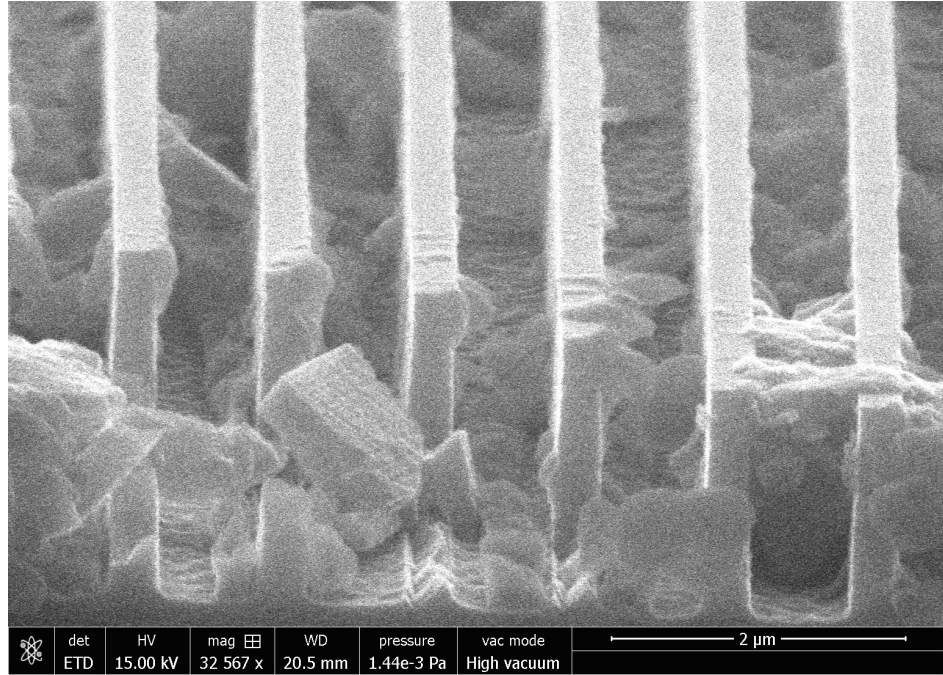


Figure 5-10: Figure showing an example of the irreparable damage caused by cleaving a structure

irreparable damage caused by cleaving is visible in [Figure 5-10](#), along with artifacts. It is important to note how straight the walls are and how rectangular the grating structure is. This is also visible in [Figure 5-11](#). The smoothness of the walls is visible in [Figure 5-12](#), where it can be clearly seen that apart from a few ( $< 10$  over  $1300\text{nm}$ ) random imperfections (on the order of  $10\text{nm}$ ) there are no repetitive scallops such as those you would normally see in a Bosch process.

At this point, the prototype master mold meets all of the constraints that were initially set. If the prototype mold were to have been cleaned more thoroughly, the resulting images would have had less artifacts. This would have been possible given more time.

### 5.3 Summary

In this chapter the EBL and DRIE processes used to fabricate the master mold were attempted and issues with these processes were addressed as they developed. The master

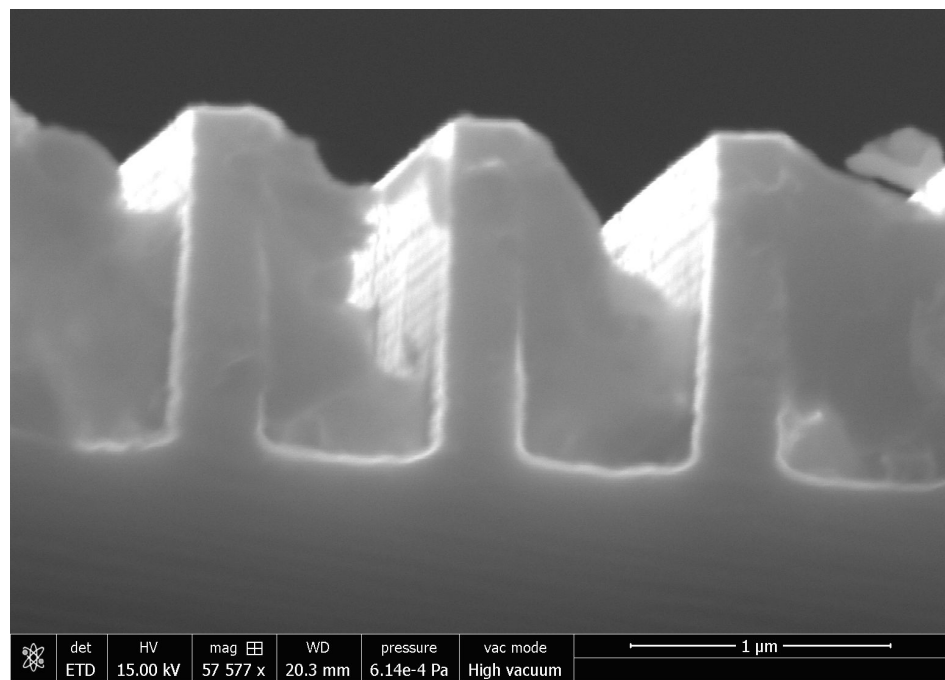


Figure 5-11: Figure showing an example of the straight walls and the rectangular grating structure generated using the Pseudo Bosch process

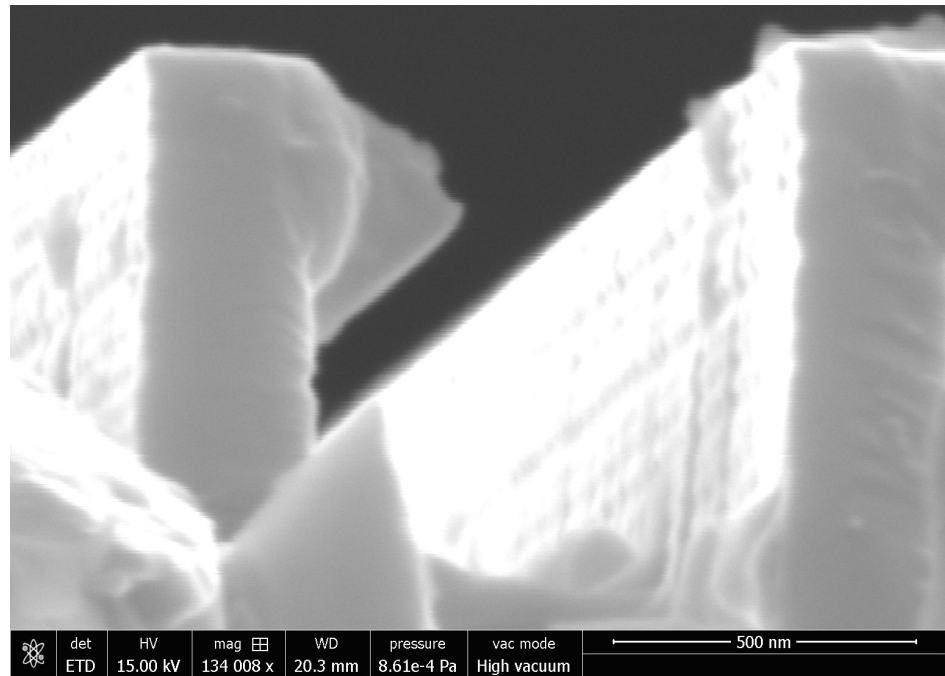


Figure 5-12: Figure showing an example of the smooth walls generated using the Pseudo Bosch process

mold that was actually fabricated could be used as a template upon which one may sputter deposit a metal to create a metal shim. This metal shim could be attached to a rotor and used to make significantly larger DGSPR devices.

The wall-e process satisfies the main constraints of the device (smooth side-walls) without resorting to a KOH wet-etch. If required the wall-e process could be performed after which a KOH step may be applied but this would require that the grating width be slightly more than  $300\text{nm}$  wide, so that after the etching process it would be exactly at  $300\text{nm}$ .

The cost of the wall-e process is appreciably below \$ 5000. The cost of the EBL is  $\sim \$250$  ( $\$87.5$  for 30 minutes of the electron beam machine and  $\$150$  for 2 hours of clean room usage) and the cost of the DRIE is around \$ 100 (for  $\sim 1$  hour of DRIE). The cost of the actual fabrication is \$350 and the cost of developing the various ad-hoc process optimizations would probably have come to less than \$5000 over the course of the year.

# Chapter 6

## Conclusion and Recommendations

In this thesis an existing design for a multi-mode Dielectric Grating based Surface Plasmon Resonance (DGSPR) sensor was optimized, with respect to production, operating considerations, and cost. To do the optimization, a simulation of the DGSPR structure was used, and the design's parameters were varied manually (within a constrained design space), keeping previously identified key manufacturing considerations in mind. Proceeding in such a manner, the 6 largest local maxima were found (within the constrained design space) and in doing so the global maxima (the largest of the local maxima) was also identified.

Based on the optimized design, a prototype master mold was fabricated using a mixture of Electron-beam lithography and Deep Reactive Ion Etching (a Pseudo Bosch process). The e-beam process was optimized to ensure that the resist was exposed at the correct beam dosage, that the proximity error correction bias term could be approximated accurately, and to ensure that the patterned Silicon/ma-N structure spent enough time in the ma-D developer. The DRIE process was also affected by issues regarding the improper development of the exposed ma-N pattern and was also optimized to ensure that the stripping process was completed correctly so as to minimize artifacts in the final structure. The final DGSPR master mold was examined under a electron microscope to determine the efficacy of the E-beam/DRIE process. The mold was found to have sufficiently smooth side-walls, and to have dimensions

within 2% of the required values.

It is theoretically possible to fabricate a larger version of the prototype mold to be used to make DGSPR sensors. An alternative is to use a smaller mold to create a metal shim which can be affixed to a rotor and used to create larger DGSPR sensors. Another alternative is to start with a small DGSPR sensor and to use micro/nano-positioners to imprint the pattern carefully onto a larger silicon wafer coated with ma-N (or some other resist) which would then be etched using the wall-e process. Suppose that in each iteration you quadrupled the size of the pattern i.e. suppose in the first iteration the pattern is on a  $100nm \times 100nm$  area, then in the second iteration it would expand to over a  $200nm \times 200nm$  square. Such a system would give you exponential growth and would be easiest way to maximize the use of the small resist. Over the course of sixteen iterations a  $100nm \times 100nm$  area can grow to an  $1\text{inch} \times 1\text{inch}$  area. The issue here is that the micro/nano-positioners have to be accurate enough to ensure that neighboring patterns do not interfere with each other. Asymptotically, if the system is sufficiently large and care is taken to ensure that the initial mold is free of any flaws, the significance of said errors should drop. Alternatively, a mix of the shim and the exponential growth idea could be used. This would definitely minimize the density of flaws in the large system. Such a system would be extremely useful for investigating statistical effects of repeated flaws (given the relatively constant density of flaws) and could be useful in the field of statistical physics/plasmonics. It would also simulate a ‘doped’ grating structure. The specific uses of this are not currently known especially since the field of quantum statistics in surface plasmon polaritons [29] is somewhat embryonic.

# Bibliography

- [1] Charles Campbell. *Surface Plasmon Resonance (SPR) Biosensor Development*. 1 edition.
- [2] Farshid Bahrami, J. Stewart Aitchison, and Mo Mojahedi. Multimode spectroscopy using dielectric grating coupled to a surface plasmon resonance sensor. *Opt. Lett.*, 39(13):3946, 2014.
- [3] Xu Wang, Wei Shi, R. Vafaei, N.A.F. Jaeger, and L. Chrostowski. Silicon-on-insulator bragg gratings fabricated by deep uv lithography. In *Communications and Photonics Conference and Exhibition (ACP), 2010 Asia*, pages 501–502, Dec 2010.
- [4] D. F. Kyser. Monte carlo simulation of spatially distributed beams in electron-beam lithography. *J. Vac. Sci. Technol.*, 12(6):1305, 1975.
- [5] Steve Zamek, Mercedeh Khajavikhan, Dawn T. H. Tan, Maurice Ayache, Boris Slutsky, and Yeshaiahu Fainman. Effects of lithographic stitching errors on the performance of waveguide bragg gratings, 2011.
- [6] M. Gnan, D. S. Macintyre, M. Sorel, R. M. De La Rue, and S. Thoms. Enhanced stitching for the fabrication of photonic structures by electron beam lithography. *Journal of Vacuum Science & Technology B: Microelectronics and Nanometer Structures*, 25(6):2034, 2007.
- [7] Yi Wen Zhang, Lei Wang, Yong Lin Yu, Ding Li Wang, Ning Zhou, and Wen Liu. High quality bragg gratings fabricated by nanoimprint lithography. *J. Phys.: Conf. Ser.*, 276:012104, 2011.
- [8] Zhaoning Yu, Lei Chen, Wei Wu, Haixiong Ge, and Stephen Y. Chou. Fabrication of nanoscale gratings with reduced line edge roughness using nanoimprint lithography. *Journal of Vacuum Science & Technology B: Microelectronics and Nanometer Structures*, 21(5):2089, 2003.
- [9] Alexandre G. Brolo. Plasmonics for future biosensors. *Nature Photonics*, 6(11):709–713, 2012.
- [10] Paolo De Paoli, Marzia Cozzi, Rosamaria Tedeschi, Annunziata Gloghini, Anna Maria Cilia, Cees van Kooten, Gianluca Gaidano, and Antonino Carbone. High cd40 membrane expression in aids-related lymphoma b cell lines is associated with the cd45ra+,

cd45ro+, cd95+ phenotype and high levels of its soluble form in culture supernatants. *Cytometry*, 30(1):33–38, 1997.

- [11] Jiri Homola, Sinclair S. Yee, and Gunter Gauglitz. Surface plasmon resonance sensors: review. *Sensors and Actuators B: Chemical*, 54(1-2):3–15, 1999.
- [12] Milan Milosevic. *Internal reflection and ATR spectroscopy*. John Wiley and amp, 2012.
- [13] Refractive index database. <http://refractiveindex.info/>. Accessed: 2015-02-08.
- [14] J. R. Sambles, G. W. Bradberry, and Fuzi Yang. Optical excitation of surface plasmons: An introduction. *Contemporary Physics*, 32(3):173–183, 1991.
- [15] Jiri Homola, Ivo Koudela, and Sinclair S. Yee. Surface plasmon resonance sensors based on diffraction gratings and prism couplers: sensitivity comparison. *Sensors and Actuators B: Chemical*, 54(1-2):16–24, 1999.
- [16] Bernard C Kress and Patrick Meyrueis. *Applied digital optics*. Wiley, 2009.
- [17] F. Bahrami, J.S. Aitchison, and M. Mojahedi. A highly optimized plasmon waveguide resonance biosensor. In *Photonics Conference (IPC), 2012 IEEE*, pages 208–209, Sept 2012.
- [18] F. Bahrami, M. Z. Alam, J. S. Aitchison, and M. Mojahedi. Dual polarization measurements in the hybrid plasmonic biosensors. *Plasmonics*, 8(2):465–473, 2012.
- [19] Greg Hughes and Henry Yun. Mask industry assessment: 2009. volume 7488, pages 748803–748803–13, 2009.
- [20] Kimberly L. Berkowski, Kyle N. Plunkett, Qing Yu, and Jeffrey S. Moore. Introduction to photolithography: Preparation of microscale polymer silhouettes. *Journal of Chemical Education*, 82(9):1365, 2005.
- [21] T. H. P. Chang. Proximity effect in electron-beam lithography. *J. Vac. Sci. Technol.*, 12(6):1271, 1975.
- [22] Richard Rau. Proximity effect correction for nanolithography. *Journal of Vacuum Science & Technology B: Microelectronics and Nanometer Structures*, 14(4):2445, 1996.
- [23] microchem.com. ma-n 2400 negative tone photoresist series.
- [24] Tnfc.utoronto.ca. ma-n 2400 series resist.
- [25] Tnfc.utoronto.ca. Electron beam lithography | tnfc | toronto nanofabrication centre.
- [26] Banqiu Wu, Ajay Kumar, and Sharma Pamarthy. High aspect ratio silicon etch: A review. *J. Appl. Phys.*, 108(5):051101, 2010.
- [27] Azonano.com. Comparison of the bosch and a cryogenically cooled deep silicon etch processes.

- [28] Tnfc.utoronto.ca. Wet & plasma etching | tnfc | toronto nanofabrication centre.
- [29] Giuliana Di Martino, Yannick Sonnefraud, Stephane Kena-Cohen, Mark Tame, Sahin K. Ozdemir, M. S. Kim, and Stefan A. Maier. Quantum statistics of surface plasmon polaritons in metallic stripe waveguides. *Nano Letters*, 12(5):2504–2508, 2012.